PTEP

Prog. Theor. Exp. Phys. **2024** 073B07 (28 pages)
DOI: 10.1093/ptep/ptae086

Probing New Physics in Light of Recent Developments in $b \to c\ell\nu$ Transitions

Tahira Yasmeen [1,⋆], Ishtiaq Ahmed [2,⋆], Saba Shafaq [1,⋆], Muhammad Arslan [3,⋆], and Muhammad Jamil Aslam [3,⋆]

[1] *Department of Physics, International Islamic University, Islamabad 44000, Pakistan*
[2] *National Center for Physics, Islamabad 44000, Pakistan*
[3] *Department of Physics, Quaid-i-Azam University, Islamabad 45320, Pakistan*
⋆E-mail: tahira709@gmail.com (T.Y.); ishtiaqmusab@gmail.com (I.A.); saba.shafaq@iiu.edu.pk (S.S.); arslan.hep@gmail.com (M.A.); jamil@qau.edu.pk (M.J.A.)

Received January 22, 2024; Revised June 1, 2024; Accepted June 12, 2024; Published June 13, 2024

Experimental studies of the observables associated with $b \to c$ transitions in semileptonic B-meson decays at BaBar, Belle, and LHCb have shown some deviations from the Standard Model predictions, consequently providing a handy tool to probe the possible new physics (NP). In this context, we first revisit the impact of recent measurements of $R(D^{(*)})$ and $R(\Lambda_c)$ on the parametric space of the NP scenarios. In addition, we include the $R(J/\psi)$ data in the analysis and find that their influence on the best-fit point and the parametric space is mild. Using the recent HFLAV data, after validating the well established sum rule of $R(\Lambda_c)$, we derive a similar sum rule for $R(J/\psi)$. Furthermore, according to the updated data, we modify the correlation among the different observables, giving us their interesting interdependence. Finally, to discriminate the various NP scenarios, we plot the different angular observables and their ratios for $B \to D^*\tau\nu_\tau$ against the transfer momentum square (q^2), using the 1σ and 2σ parametric space of considered NP scenarios. By implementing the collider bounds on NP Wilson coefficients (WCs), we find that the parametric space of some NP WCs is significantly restrained. To see the clear influence of NP on the amplitude of the angular observables, we also calculate their numerical values in different q^2 bins and show them through bar plots. We hope that their precise measurements will help to discriminate various NP scenarios.

Subject Index B51, B52, B56, B57

1. Introduction

The Standard Model (SM) of particle physics has successfully explained most of the experimental measurements; however, in semileptonic B-meson decays, 2σ–4σ-level deviations from SM predictions have been observed in recent measurements of $R(D^{(*)})$, $R(J/\psi)$, and the τ polarization asymmetry [1–14]. These observables belong to the $b \to c\ell\nu_\ell$ transitions occurring through flavor-changing charged current (FCCC). Therefore, the observables belonging to the FCCC transitions are an excellent tool to check the SM predictions and to hunt for physics beyond it, i.e. New Physics (NP).

As we know, the theoretical predictions for the decay rates of semileptonic decays show hadronic uncertainties mainly arising due to the form factors (nonperturbative quantities) and from Cabibbo–Kobayashi–Maskawa (CKM) matrix elements. However, in the ratios such as $R(D^{(*)})$ [15–17], $R(J/\psi)$ [18,19], $R(X_c)$ [20–22], and $\mathcal{R}(\Lambda_c)$ [23,24], the dependence on the CKM elements and on the form factor cancels out. From the experimental point of view, the ratios

Table 1. Different physical observables, with their experimental measurements and SM predictions.

Observables	SM predictions	Experimental measurements
$R(D)$	0.298 ± 0.004 [33]	0.344 ± 0.026 HFLAV [33]
$R(D^*)$	0.254 ± 0.005 [33]	0.285 ± 0.012 HFLAV [33]
$P_\tau(D^*)$	-0.497 ± 0.007 [42]	$-0.38 \pm 0.51^{+0.21}_{-0.16}$ [40,41]
$F_L(D^*)$	0.464 ± 0.003 [64]	$0.60 \pm 0.08 \pm 0.04$ [16]
$R(J/\psi)$	0.258 ± 0.038 [65,66],	$0.71 \pm 0.17 \pm 0.18$ [18]
$R(\Lambda_c)$	0.324 ± 0.004 [2]	$0.242 \pm 0.026 \pm 0.040 \pm 0.059$ [67]

$R(D^{(*)})$, are measured by the BaBar [25,26], Belle [27–30], and LHCb [31,32] collaborations and the latest value of the HFLAV world average [33] shows an approximately 3.3σ deviation from its SM prediction [25,26,34–39]. The other such observables are the ratios of the decay rates of the B meson decaying to polarized and unpolarized final-state mesons, i.e. $P_\tau(D^*)$ and $F_L(D^*)$. Their measurements at Belle reported 1.5–2 σ deviation from their SM results [40–45]. In particular, $F_L(D^*)$ is important in probing different NP scenarios because the D^* polarizations help us to distinguish between different Lorentz structures (scalar, vector, and tensor operators) that influence its value [1]. Similarly, the observable $R(J/\psi)$ has around 2σ deviation from its SM value $\approx$ 0.23–0.29 [46–52]. Although its form factors are not precisely known, to see its current impact on the parametric space, we have included this observable in our analysis. Additionally, like $R(D^{(*)})$, the LHCb Collaboration [23] has recently measured $\mathcal{R}(\Lambda_c)$ in $\Lambda_b \to \Lambda_c \tau^- \bar{\nu}_\tau$ decays. Its opposite behavior compared to $R(D^{(*)})$ has triggered a lot of theoretical interest; see e.g. Ref. [2] for an updated discussion. Finally, because of the lack of accurate measurement of the branching ratio of $B_c^- \to \tau^- \nu$ decay, the lifetime of the B_c meson has put some stringent constraints on the possible NP parameters [43,53–56]. In this work, for the χ^2 analysis we have used the recent measurements, given in Table 1, of the six observables discussed above, i.e. $R(D^{(*)})$, $P_\tau(D^*)$, $F_L(D^*)$, $R(J/\psi)$, and $\mathcal{R}(\Lambda_c)$. For the unobserved decay $B_c^- \to \tau^- \nu$, we use the 10%, 30%, and 60% upper limits on its branching ratio [57–63] in our analysis.

Perhaps it is useful to mention that in the earlier attempts the constraints on the parametric space of NP Wilson coefficients (WCs) were obtained by considering only the vector or scalar contributions separately [68–74]. However, Blanke et al. have done a comprehensive analysis by considering scalar, vector, and tensor couplings, but by using only the four experimentally measured observables, namely, $R(D^{(*)})$, $P_\tau(D^*)$, and $F_L(D^*)$[1]. Including the recent measurement of $R(\Lambda_c)$, this analysis was revised by Fedele et al. [2].

The situation is robustly changing; theoretically, we have better control over the uncertainties of the form factors of $B \to D^{(*)}$ [75,64] decay and, experimentally, after the recent measurements of Belle [76] and LHCb [77,78], HFLAV [33] updated their earlier results accordingly. In addition, it will be interesting to redo the analysis by considering these updated values along with the measurements of $R(J/\psi)$ and $R(\Lambda_c)$. For this purpose, we include all the observables mentioned above together with their updated measurements in our fit analysis; these are absent in previous studies [1,2,68–74].

With this motivation, the main purpose of this work is not only to explore the allowed parametric space according to the current situation regarding $b \to c$ transitions but also to see the sensitivity of some angular observables to the NP models, which may provide a tool to discriminate among different NP scenarios. To achieve this, we analyze the CP-even angular observables in $B \to D^* \ell \nu_\ell$ decays, and to see their sensitivity on the NP couplings we plotted them against the invariant dilepton mass q^2. We would like to mention here that LHC analysis of high-pT mono-τ searches with missing transverse energy searches has also given upper limits on the NP WCs, so we have imposed these upper limits on the considered NP scenarios. We have also calculated their numerical values both in different q^2 bins and in the full q^2 region.

Scheme of our analysis: Some benchmarks of the current analysis are described as follows:

- To accomplish the goal discussed above, we extend the SM weak effective Hamiltonian (WEH) for the charged current $b \to c\tau\nu$ by adding the new scalar, vector, and tensor type contributions.
- In the current study, the analysis has been done at 2 TeV by using the latest data of all available observables $R(D^{(*)})$, $R(J/\psi)$, $F_L(D^*)$, $P_\tau(D^*)$, and $\mathcal{R}(\Lambda_c)$. In addition, for comparison with Blanke et al., plots at 1 TeV with updated measurements are also shown. The recipe for the analysis is similar to that of Blanke et al. [1].
- Based on the choice of observables used for the fitting analysis for NP couplings, we consider the following cases:
  - Fit A: $R(D^{(*)})$, $F_L(D^*)$, $P_\tau(D^*)$
  - Fit B: $R(D^{(*)})$, $F_L(D^*)$, $P_\tau(D^*)$, $R(J/\psi)$,
  - Fit C: $R(D^{(*)})$, $F_L(D^*)$, $P_\tau(D^*)$, $R(J/\psi)$, $\mathcal{R}(\Lambda_c)$
- We validate the sum rule of $R(\Lambda_c)$ [1,2], and update it by including the recent theoretical and experimental developments. Similarly, there is a large uncertainty in the value of $R(J/\psi) = 0.71 \pm 0.17 \pm 0.18$ measured by the LHCb Collaboration [18] and to support the future experimental value with its theoretical predicted value 0.23–0.29, we have also discussed the sum rule of $R(J/\psi)$ in terms of $R(D^{(*)})$.
- Furthermore, to see the discriminatory power of the observables under consideration, we have also found the correlation among different observables as a function of $R(D^{(*)})$ in different 2D NP scenarios.
- Finally, using the 1σ and 2σ intervals of the NP couplings, we will calculate the numerical values of various CP-even observables in $B \to D^* \tau \nu_\tau$ decay [44,72,79–81] and discuss their potential to segregate different NP scenarios. We also show bar plots of these angular observables in different bins.

This paper is organized as follows: In Section 2, after giving the effective Hamiltonian, we have listed the analytical expressions for the considered observables as a function of NP WCs. The fitting procedure that is used to get the allowed values of different NP WCs has also been discussed in the same section. Section 3 discusses 1D and 2D NP scenarios and their phenomenological analysis of the parametric space with and without considering the collider LHC bounds. The correlation among the observables and the sum rules are discussed in Section 4. In Section 5, we check the sensitivity of CP-even angular observables for different NP scenarios and compare their values with the corresponding SM predictions by plotting them against q^2 taking into account the LHC bounds. Finally, bar plots are drawn to show their numerical values in different q^2 bins.

2. Theoretical formulation

At the quark level, we consider the following WEH for $b \to c\ell\bar{\nu}_\ell$ transitions:

$$\mathcal{H}_{\text{eff}}^{b\to c\ell\bar{\nu}_\ell} = \frac{4G_F}{\sqrt{2}} V_{cb}\big[\left(1 + C_V^L\right)\mathcal{O}_V^L + C_V^R\mathcal{O}_V^R + C_S^R\mathcal{O}_S^R + C_S^L\mathcal{O}_S^L + C_T\mathcal{O}_T\big] + \text{h.c.}, \tag{1}$$

where $\ell = \mu, \tau$, G_F is the Fermi constant, V_{cb} is the CKM matrix element, and C_i^X are the new WCs with $i = V, S, T$ and $X = L, R$. The corresponding quark-level operators $\mathcal{O}_i^X$ are

$$\begin{aligned}
&\mathcal{O}_S^L = (\bar{c}P_L b)\left(\bar{\ell}P_L\nu\right), && \mathcal{O}_S^R = (\bar{c}P_R b)\left(\bar{\ell}P_L\nu\right),\\
&\mathcal{O}_V^L = (\bar{c}\gamma^\mu P_L b)\left(\bar{\ell}\gamma_\mu P_L\nu\right), && \mathcal{O}_V^R = (\bar{c}\gamma^\mu P_R b)\left(\bar{\ell}\gamma_\mu P_L\nu\right),\\
&\mathcal{O}_T = (\bar{c}\sigma^{\mu\nu} P_L b)\left(\bar{\ell}\sigma_{\mu\nu} P_L\nu\right),
\end{aligned} \tag{2}$$

with $P_L = \frac{1-\gamma_5}{2}$ and $P_R = \frac{1+\gamma_5}{2}$. We know that experimentally no new states beyond the SM have been found so far up to an energy scale of approximately 1 TeV. Also, the measurements of the Higgs couplings are all consistent with the SM expectations; therefore the right-handed operators do not contribute in the SM [82], making the coupling C_V^R universal, which is strongly constrained from $b \to c(e, \mu)\bar{\nu}_{(e,\mu)}$ data. However, if the assumption of linearity of electroweak symmetry breaking is relaxed then one can consider a nonuniversal C_V^R coupling in the analysis; we therefore included it and discuss this case separately in our analysis (see Refs. [82,83] for details). Moreover, in the absence of experimental evidence of deviations from the SM in tree-level transitions involving light leptons, the NP effects are generally supposed to appear in the third generation of leptons [82].

The new WCs present in Eq. (1) are calculated at 2 TeV, and these are related to the $\mu = m_b$ scale as follows [84]:

$$\begin{gathered}
C_V^L(m_b) = 1.12C_V^L(2\,\text{TeV}), \quad C_V^R(m_b) = 1.07C_V^R(2\,\text{TeV}), \quad C_S^R(m_b) = 2C_S^R(2\,\text{TeV}),\\
\begin{pmatrix} C_S^L(m_b) \\ C_T(m_b) \end{pmatrix} = \begin{pmatrix} 1.91 & -0.38 \\ 0 & 0.89 \end{pmatrix} \begin{pmatrix} C_S^L(2\,\text{TeV}) \\ C_T(2\,\text{TeV}) \end{pmatrix}.
\end{gathered} \tag{3}$$

2.1. *Analytical expressions of the observables*

By sandwiching the WEH given in Eq. (1), the analytical expressions of the ratios $R(D^{(*)})$, $R(J/\psi)$, and the observables depend on the polarization of final-state particles; $F_L(D^*)$, $P_\tau(D)$, and $P_\tau(D^*)$ can be parametrized in terms of NP WCs as follows [24,43,47,55,56,73,74,64,82,85]:

$$\begin{aligned}
R(D) = R_D^{\text{SM}}\Big\{&\left|1 + C_V^L + C_V^R\right|^2 + 1.01\left|C_S^R + C_S^L\right|^2 + 1.49\text{Re}\big[\left(1 + C_V^L + C_V^R\right)\left(C_S^R + C_S^L\right)^*\big]\\
&+0.84\left|C_T\right|^2 + 1.08\text{Re}\big[\left(1 + C_V^L + C_V^R\right)(C_T)^*\big]\Big\},
\end{aligned} \tag{4}$$

$$\begin{aligned}
R(D^*) = R_{D^*}^{\text{SM}}\Big\{&\left|1 + C_V^L\right|^2 + \left|C_V^R\right|^2 + 0.04\left|C_S^L - C_S^R\right|^2 + 16.0\left|C_T\right|^2 - 1.83\text{Re}\big[\left(1 + C_V^L\right)C_V^{R^*}\big]\\
&+6.60\text{Re}[\left(C_V^R\right)C_T^*] - 5.17\text{Re}\big[\left(1 + C_V^L\right)C_T^*\big]\\
&+0.11\text{Re}\big[\left(1 + C_V^L - C_V^R\right)\left(C_S^R - C_S^L\right)^*\big]\Big\},
\end{aligned} \tag{5}$$

$$F_L(D^*) = F_L(D^*)^{\rm SM}\left(\frac{R_{D^*}}{R_{D^*}^{\rm SM}}\right)^{-1}\Big\{\left|1 + C_V^L - C_V^R\right|^2 + 0.08\left|C_S^L - C_S^R\right|^2 + 6.90\left|C_T\right|^2$$
$$-0.25{\rm Re}\big[\left(1 + C_V^L - C_V^R\right)\left(C_S^L - C_S^R\right)^*\big] - 4.30{\rm Re}\big[\left(1 + C_V^L - C_V^R\right)C_T^*\big]\Big\}, \quad (6)$$

$$P_\tau(D)^* = P_\tau(D^*)^{\rm SM}\left(\frac{R_{D^*}}{R_{D^*}^{\rm SM}}\right)^{-1}\Big\{\left|1 + C_V^L\right|^2 + \left|C_V^R\right|^2 - 0.07\left(\left|C_S^R - C_S^L\right|^2\right) - 1.85\left|C_T\right|^2$$
$$+0.23{\rm Re}\big[\left(1 + C_V^L - C_V^R\right)\left(C_S^L - C_S^R\right)^*\big] - 1.79{\rm Re}\big[\left(1 + C_V^L\right)C_V^{R^*}\big]$$
$$-3.47{\rm Re}\big[\left(1 + C_V^L\right)C_T^*\big] + 4.41{\rm Re}\big[\left(C_V^R\right)C_T^*\big]\Big\}, \quad (7)$$

$$P_\tau(D) = P_\tau(D)^{\rm SM}\left(\frac{R_{D^*}}{R_{D^*}^{\rm SM}}\right)^{-1}\Big\{\left|1 + C_V^L + C_V^R\right|^2 + 3.04\left(\left|C_S^R + C_S^L\right|^2\right) + 0.17\left|C_T\right|^2$$
$$+4.50{\rm Re}\big[\left(1 + C_V^L + C_V^R\right)\left(C_S^L + C_S^R\right)^*\big] - 1.09{\rm Re}\big[\left(1 + C_V^L + C_V^{R^*}\right)C_T^*\big], \quad (8)$$

$$R(J/\psi) = R(J/\psi)^{\rm SM}\Big\{\left|1 + C_V^L\right|^2 + \left|C_V^R\right|^2 - 1.82{\rm Re}\big[\left(1 + C_V^L\right)C_V^{R*}\big] + 0.04\left(\left|C_S^L - C_S^R\right|^2\right)$$
$$+0.10{\rm Re}\big[\left(1 + C_V^L - C_V^R\right)\left(C_S^R - C_S^L\right)^*\big] + 14.7\left|C_T\right|^2 - 5.39{\rm Re}\big[\left(1 + C_V^L\right)C_T^*\big]$$
$$+6.57{\rm Re}\big[\left(C_V^R\right)C_T^*\big]\Big\}, \quad (9)$$

$$\mathcal{R}(\Lambda_c) = \mathcal{R}(\Lambda_c)^{\rm SM}\Big\{\left|1 + C_V^L\right|^2 + \left|C_V^R\right|^2 + 0.491{\rm Re}\big[\left(1 + C_V^L\right)C_S^{R*}\big] + 0.316\big[\left(1 + C_V^L\right)C_S^{L*}\big]$$
$$+0.484\big[\left(C_S^L\right)C_S^{R*}\big] + 0.31\left(\left|C_S^L\right|^2 + \left|C_S^R\right|^2\right) - 2.96{\rm Re}\big[\left(1 + C_V^L\right)C_T^*\big] + 10.52\left|C_T\right|^2$$
$$-0.678{\rm Re}\big[\left(1 + C_V^L\right)C_V^{R*}\big] + 0.316{\rm Re}\big[\left(C_S^R\right)C_V^{R*}\big] + 0.491{\rm Re}\big[\left(C_S^L\right)C_V^{R*}\big]$$
$$+4.85{\rm Re}\big[\left(C_V^R\right)C_T^*\big]\Big\}. \quad (10)$$

Similarly, the branching ratio of $B_c \to \tau\nu$ decay can take the form [10,54,57,58]:

$$\frac{Br(B_c \to \tau\nu)}{Br(B_c \to \tau\nu)|_{\rm SM}} = \left|1 + \left(C_V^L - C_V^R\right) + \frac{m_{B_c}^2}{m_\tau(m_b + m_c)}\left(C_S^R - C_S^L\right)\right|^2. \quad (11)$$

2.2. *Fit procedure*

The standard χ^2 analysis of the aforementioned observables for the decays governed by $b \to c\tau\nu$ transitions can be done by using

$$\chi^2\left(C_i^X\right) = \sum_{l,m}^{N_{\rm obs}}\left[O_l^{\rm exp} - O_l^{\rm th}\left(C_i^X\right)\right]C_{lm}^{-1}\left[O_m^{\rm exp} - O_m^{\rm th}\left(C_i^X\right)\right],$$

where $N_{\rm obs}$ represents the number of observables, $O_l^{\rm exp(th)}$ are the experimental (theoretical) values of the observables, and C_i^X are the NP WCs. C_{lm} is the covariance matrix incorporating the theoretical and experimental uncertainties. However, instead of using the covariance matrix, the χ^2 function can be written in the form of pulls, i.e. $\chi^2 = \sum_i^{N_{\rm obs}}({\rm pull}_i)^2$, where

$\text{pull}_i = (O^i_{\text{exp}} - O^i_{\text{th}})/\sqrt{\sigma^{i2}_{\text{exp}} + \sigma^{i2}_{\text{th}}}$. Here $\sigma^i_{\text{exp(th)}}$ shows the experimental (theoretical) error that is added in quadrature. The correlation of $R(D)$ and $R(D^*)$ has been taken into account by using the following relation:

$$\chi^2_{R(D)-R(D^*)} = \frac{\text{pull}(R(D))^2 + \text{pull}(R(D^*))^2 - 2\rho\text{pull}(R(D))\text{pull}(R(D^*))}{(1-\rho^2)}.$$

The latest value for the $R(D) - R(D^*)$ correlation reported in Ref. [33] is $\rho = -0.39$, and for the uncorrelated observables, this value is zero.

For analysis, using latest data reported by HFLAV (cf. Table 1), we first calculate the best-fit points by minimizing the χ^2 function (χ^2_{min}) in the region of parametric space that is compatible with the upper bound of $BR(B_c \to \tau\nu) < 60\%$, $< 30\%$, and $< 10\%$ [73]. χ^2_{min} is thus used to evaluate the p-values, which are a measure of the goodness of fit allowing us to quantify the level of agreement between the data and the NP scenarios [1,3,69]. The number of degrees of freedom (dof), $N_{\text{dof}} = N_{\text{obs}} - N_{\text{par}}$, where $N_{\text{par}} = 1(2)$ for the 1D (2D) scenarios while the number of observables, N_{obs}, is the number of observables used in the fitting, i.e. N_{obs} is 4, 5, and 6 for Fits A, B, and C, respectively. The SM pull is defined as $\text{pull}_{\text{SM}} = \chi^2_{\text{SM}} - \chi^2_{\text{min}}$, where $\chi^2_{\text{SM}} = \chi^2(0)$, which can be converted into an equivalent significance in units of standard deviations (σ).

2.3. *Specific NP scenarios influenced by leptoquark (LQ) models*

Among the different NP models, LQ models have recently gained attention to solve the B-physics anomalies; therefore, in this study, we consider different 1D and 2D scenarios of LQ models as discussed in Refs. [12,42,86–130]:

- For 1D scenarios: C^L_V, C^L_S, C^R_S, $C^L_S = 4C_T$,
- For 2D scenarios: (C^L_V, $C^L_S = -4C_T$), (C^L_S, C^R_S), (C^L_V, C^R_S), (Re[$C^L_S = 4C_T$], Im[$C^L_S = 4C_T$]).

The combinations arising from the C^R_V term will be discussed in the upcoming section separately.

3. Allowed parametric space in 1D and 2D LQ scenarios

In this section, we perform a χ^2 analysis of above-mentioned 1D and 2D LQ scenarios with the latest HFLAV data, and by using the fitting procedure discussed in the previous section.

3.1. *1D scenarios*

In Fig. 1, we show the χ^2 dependence on the SM and NP WCs for 1D scenarios at 1 and 2 TeV scales. The dashed vertical lines correspond to the constraints on C^X_i from the different upper bounds of $BR(B_c \to \tau\nu)$. The dotted, dashed, and solid curves represent the cases of Fits A, B, and C, respectively. From Fig. 1, one can notice that the positive best-fit points of the NP models are not significantly changed with respect to the scales of new WCs, while the negative best-fit points and the vertical lines of $BR(B_c \to \tau\nu)$ are slightly shifted to the right. It can also be noticed that the updated data indicate that the negative solutions of the best-fit points for C^L_S and C^R_S are still excluded by the maximum upper limit of $BR(B_c \to \tau\nu) \leq 60\%$ as reported by Blanke et al. [1,3], and this is also disfavored with respect to their SM values. One can also see from the plot that near the positive best-fit point, C^L_V and C^R_S are still favorable to explain the data, while the favorable situation of C^L_S is further improved with the new data.

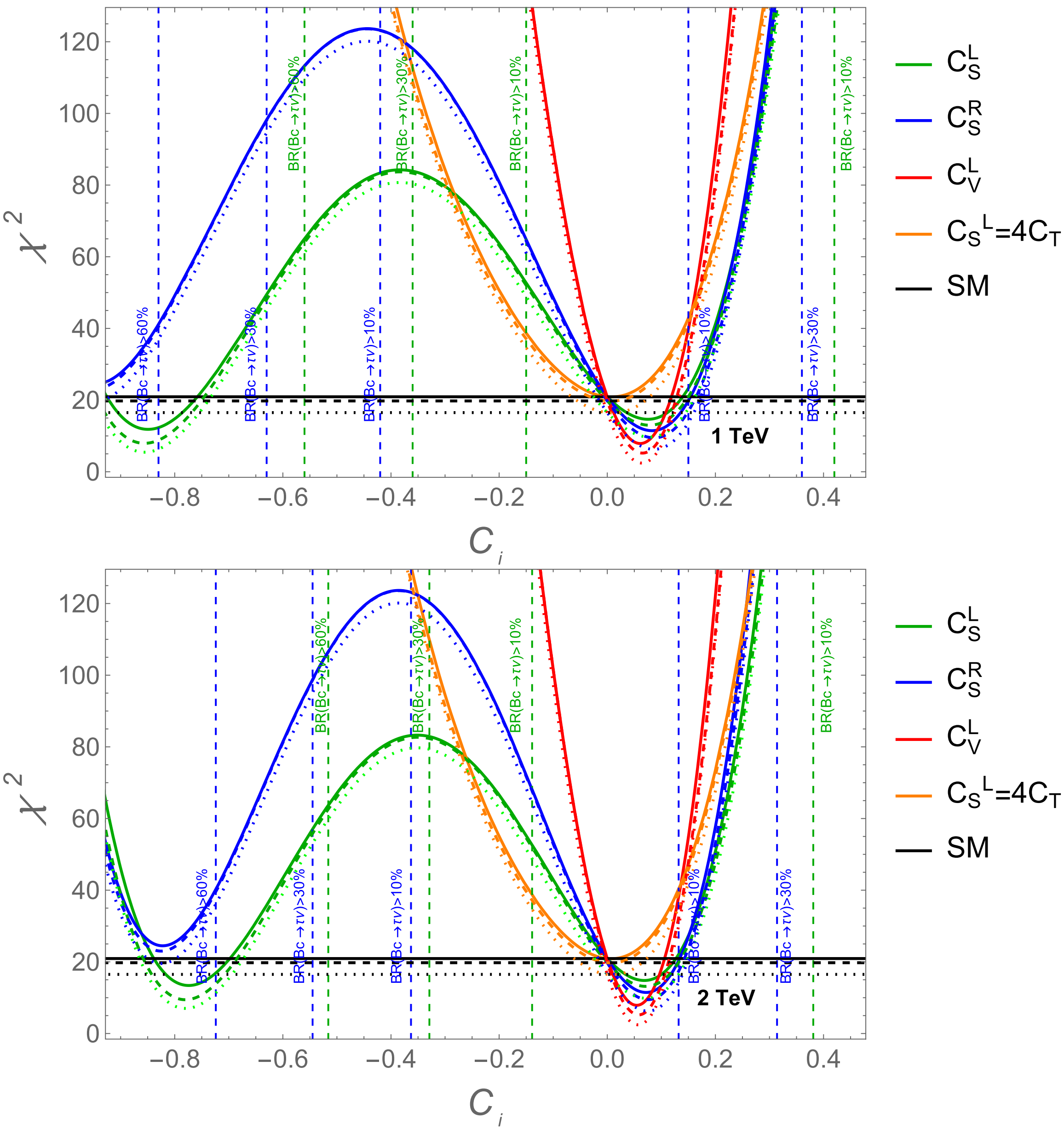

Fig. 1. Dependence of χ^2 with one Wilson coefficient active at a time for different fits at 1 and 2 TeV scales. The colored dotted, dashed, and solid lines represent Fits A, B, and C, respectively, while the black lines represent their SM values. The dashed vertical lines correspond to the constraint for $C_S^{L,R}$ from $B_c \to \tau\nu$ assuming values of 10%, 30%, and 60%.

In columns 2–5 of Table 2, we list the numerical values of the best-fit points, $\chi^2_{\rm min}$, p-value, and pull$_{\rm SM}$ in different fits for 1D scenarios. Here the first, second, and third rows represent Fits A, B, and C, respectively. The last seven columns show the predictions of different observables at the best-fit point with the σ deviation. $\chi^2_{\rm SM}$ and p-value are also given at the top of Table 2 for all fits. It is worth mentioning here that we have calculated these numerical values on both 1 and 2 TeV scales and found that the values are not significantly changed.

The slight dependence of the best-fit point of C_S^R (see Table 1 of Ref. [1]) on $BR(B_c \to \tau\nu)$ has also disappeared for the new data. The p-values, pull$_{\rm SM}$, and predictions of different observables for 1D scenarios are also tabulated in Table 2. The 1σ and 2σ intervals for WCs have also been

Table 2. Fit results for 1D scenarios using all available data. The best-fit points, $\chi^2_{\min}$, p-value, pull$_{\rm SM}$ are given. Columns 2–5 represent the results for different parameters: The first, second, and third rows in these columns represent Fits A, B, and C, respectively. The last seven columns show the predictions of different observables at the best-fit point with the σ deviation. $\chi^2_{\rm SM}$ and p-value are also given at the top of the table for all fits.

$\chi^2_{\rm SM} = (16.50, 19.76, 20.92)_{A,B,C}$, p-value $= (2.41, 1.38, 1.89)_{A,B,C} \times 10^{-3}$											
Scenarios	Best fit	$\chi^2_{\min}$	p-value %	pull$_{\rm SM}$	$R(D)$	$R(D^*)$	$R(J/\psi)$	$F_L(D^*)$	$P_\tau(D^*)$	$P_\tau(D)$	$R(\Lambda_c)$
C_S^L	0.07	9.85	1.98	2.58	0.362	0.250	0.254	0.455	-0.518	0.489	0.339
		13.16	1.03	2.56	0.69σ	-2.91σ	-1.84σ	-1.62σ	-0.25σ		1.27σ
		14.80	1.12	2.47							
C_S^R	0.07	6.26	9.96	3.20	0.366	0.258	0.261	0.473	-0.472	0.498	0.348
	0.08	9.46	5.05	3.21	0.85σ	-2.25σ	-1.83σ	-1.42σ	-0.17σ		1.39σ
	0.07	11.46	4.29	3.07							
C_V^L	0.06	2.43	48.8	3.75	0.332	0.283	0.287	0.464	-0.497	0.331	0.361
	0.06	5.20	26.7	3.82	-0.46σ	-0.17σ	-1.71σ	-1.52σ	-0.21σ		1.57σ
	0.05	7.87	16.4	3.61							
C_V^R	-0.04	13.62	0.35	1.69	0.273	0.274	0.278	0.467	-0.496	0.331	0.333
	-0.05	16.54	0.24	1.79	-2.73σ	-0.92σ	-1.74σ	-1.49σ	-0.21σ		1.19σ
	-0.04	18.05	0.28	1.69							
$C_S^L = 4C_T$	0.009	16.41	0.09	0.30	0.304	0.251	0.255	0.463	-0.500	0.341	0.323
	0.007	19.71	0.06	0.22	-1.53σ	-2.83σ	-1.83σ	-1.53σ	-0.22σ		1.07σ
	0.007	20.87	0.08	0.22							

calculated and are listed in Table 4 later. One can see that the p-values for all 1D scenarios are improved by considering the new experimental data, particularly for C_V^L (C_S^R). These two scenarios are significantly enhanced and moved up to 48.8% (9.96%) for Fit A ($N_{\rm obs} = 4$), which previously found to be 35% ($\simeq 2\%$) [1]. This shows that C_V^L (C_S^R) is still favorable. Despite the slight improvement in the p-value of $C_S^L = 4C_T = (0.06 - 0.09)\%$, this scenario still describes the data poorly.

We can see from Table 2 that with increasing the number of observables, $\chi^2_{\min}$ (p-value) is increased (decreased); consequently, the pull is reduced with all fit cases under consideration except C_V^R. This indicates that the p-value decreases, i.e. the goodness of fit is reduced, when we include the data of $R(J/\psi)$ and $R(\Lambda_c)$ in the analysis, except for the scenarios (C_S^L, $C_S^L = 4C_T$). This is attributed to the large experimental uncertainty in the measurement of $R(J/\psi)$ and the inconsistency of the measurement of $R(\Lambda_c)$ with respect to $R(D^{(*)})$.

For the best-fit points of the NP scenario the theoretically predicted values of the observables are given in Table 2 (last seven columns). Using the relation [1]

$$d_{O_i} = \frac{O_i^{\rm NP} - O_i^{\rm exp}}{\sigma^{O_i^{\rm exp}}}, \tag{12}$$

endequation∗

we have also tabulated their discrepancies from the corresponding experimental values. The results can be concluded from the above table as follows: For $R(D)$ and $P_\tau(D^*)$ the deviations are found to be less than 1σ for all NP scenarios except $R(D)$ in the $C_S^L = 4C_T$ (C_V^R) scenario, where it is found to be -1.53σ (-2.73σ). On the other hand, for the observables $R(D^*)$, $R(J/\psi)$, $F_L(D^*)$, and $R(\Lambda_c)$, the deviations are between 1 and 3σ, except for $R(D^*)$ in C_V^L, which is -0.17σ. It is also important to mention here that the values of these observables are mildly affected by changing $N_{\rm obs}$ in the analysis.

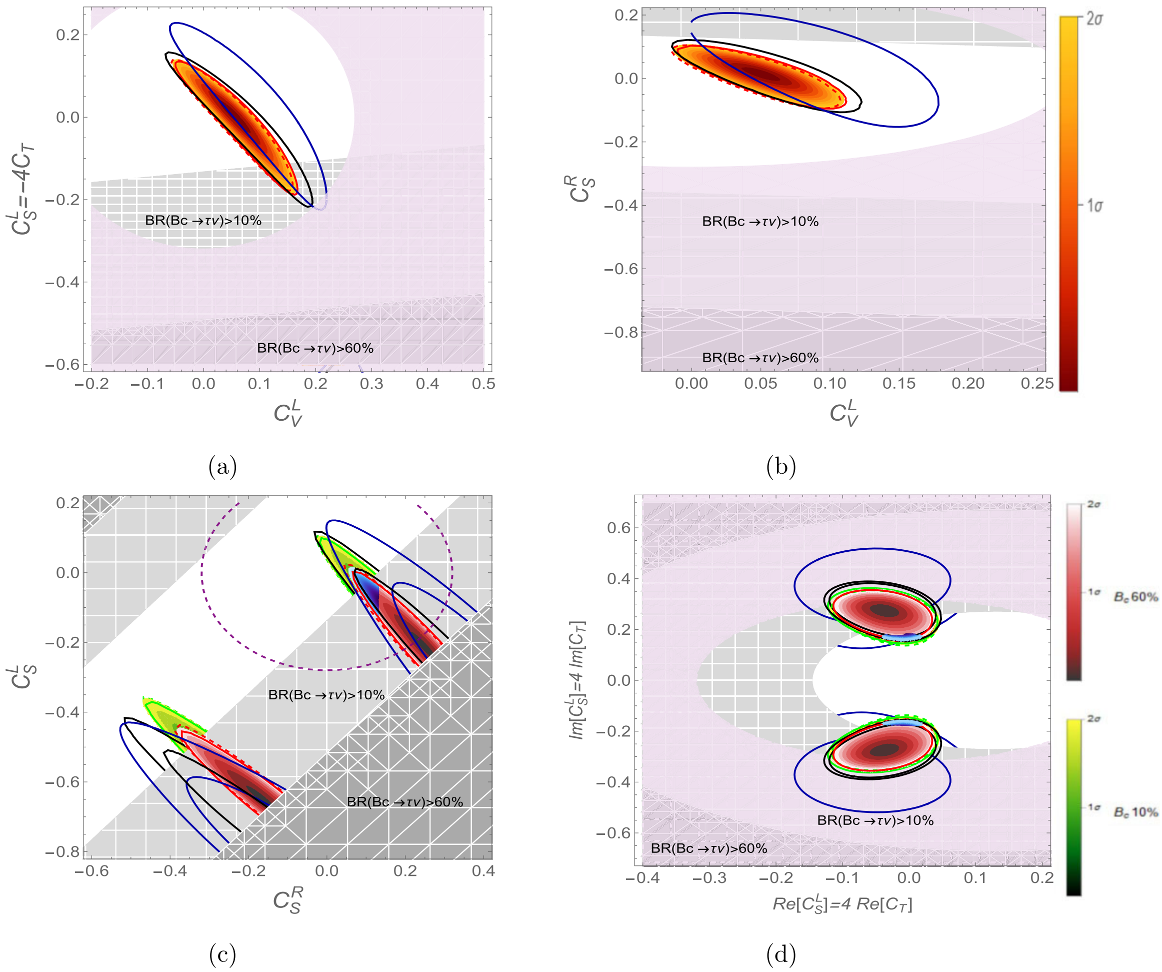

Fig. 2. Results of the fits for 2D NP scenarios. The light and dark gray regions show the 10% and 60% branching ratio constraints. The light (dark) shaded contours represent the 1σ (2σ) intervals. Panels (a), (b), (c), and (d) show the (C_V^L, $C_S^L = -4C_T$), (C_V^L, C_S^R), (C_S^R, C_S^L), and (Re[$C_S^L = 4C_T$], Im[$C_S^L = 4C_T$]) scenarios, respectively. The shaded contours represent Fit A, solid contours represent Fit B, and the dashed contours represent Fit C. The red and green colors in Figs. 1c and 1d show the allowed parametric regions when the branching ratio constraints are taken to be 60% and 10%, respectively. The blue (black) contours show the results by using the previous (new) data of $R(D^{(*)})$ at 1 TeV. The purple shaded regions shows the excluded current collider bounds at the 2σ level. The dashed purple circle in plot (c) represents the collider constraint on the charged Higgs scenario and the shaded blue color shows the LHC future bounds.

3.2. *2D scenarios*

In this section, we will perform a phenomenological analysis of the 2D NP scenarios that are defined in Section 2.3, which are generated by exchanging a single new LQ or a Higgs particle. In this case, for the χ^2 analysis, we have considered $N_{\rm par} = 2$.

In Fig. 2, we have plotted the 1σ and 2σ allowed parametric space in the 2D NP scenario planes. The shaded colored regions (the black contours) represent at 2 TeV (1 TeV) the allowed parametric space for Fit A, while the solid red and dashed contours are for Fits B and C, respectively. Moreover, in Fig. 2, for comparison with Ref. [1], we have also shown the allowed parametric regions by the blue contours for NP scenarios for Fit A where the authors of Ref. [1] considered the old data for the observables. The gray hatched regions are excluded by the 60% and 10% upper limits on the branching ratio of $B_c \to \tau\nu$. From the plots of Fig. 2, one can easily see the change in the allowed parametric space by changing the scale of NP WCs from 1 TeV to 2 TeV and by the updated data. We can observe that, by using the updated data and shifting the scale of the NP WCs from low to high, we squeeze the allowed parametric space of NP scenarios.

It can be noted from Fig. 2a that the allowed parametric space for scenario ($C_V^L, C_S^L = -4C_T$) for Fit A (orange shaded region) is not greatly affected whether we include the $R(J/\psi)$ (Fit B (red solid contour)) or by inclusion of $R(J/\psi)$ and $R(\Lambda_c)$ together (Fit C (red dashed contour)) in the analysis. On the other hand, in the scenario (C_V^L, C_S^R), the allowed parametric space is affected by neither $B_c \to \tau\nu$ nor by the number of observables and remains approximately the same for Fits A, B, and C. Figures 2c and 2d depict the allowed parametric space for scenarios (C_S^L, C_S^R) and (Re[$C_S^L = 4C_T$, Im[$C_S^L = 4C_T$]), respectively, where the red (green) shaded region represents $B_c \to \tau\nu \leq 60\%$ ($\leq 10\%$). From these figures, one can see that for both these scenarios the allowed parametric space at $B_c \to \tau\nu \leq 10\%$ remains almost the same for Fits A, B, and C. On the other hand, at $B_c \to \tau\nu \leq 60\%$, the parametric space is elongated for Fit C (red dashed contour).

By applying the upper limits of $BR(B_c \to \tau\nu) < 60\%$, $< 30\%$, and $< 10\%$, the results for the different parameters of 2D scenarios for Fits A, B, and C are given in Table 3. One can observe that, for all the fitting cases, the best-fit points of scenarios ($C_V^L, C_S^L = -4C_T$) and (C_V^L, C_S^R) are not affected by $BR(B_c \to \tau\nu)$, but this not the case for the other two scenarios, (C_S^L, C_S^R) and (Re[$C_S^L = 4C_T$, Im[$C_S^L = 4C_T$]), as also mentioned in Ref. [1]. However, by using the updated data for Fit A, the goodness of fit (p-value) increases $\sim 4\%$ ($22\% \to 29.8\%$) for ($C_V^L, C_S^L = -4C_T$) and $\sim 2\%$ ($30.8\% \to 31.8\%$) for (C_V^L, C_S^R). Here, one can also notice from Fig. 2c that the NP scenario (C_S^L, C_S^R) is significantly affected by the WC scale as compared to the other three scenarios. Therefore, for (C_S^L, C_S^R), by setting $BR(B_c \to \tau\nu) < (10, 30, 60)\,\%$ the p-values are increased $\sim (9, 34, 3)\,\%$ at 2 TeV and $\sim (9, 28, 7)\,\%$ at 1 TeV, respectively.

Therefore, the updated data indicate that the scenario (C_S^L, C_S^R) with the hard cut $BR(B_c \to \tau\nu) < 30\%$ is also favorable. The variation in p-value for the scenario (Re[$C_S^L = 4C_T$, Im[$C_S^L = 4C_T$]) has improved; as for $BR(B_c \to \tau\nu) < 60\%$ and $< 30\%$, the p-value is increased from $22\% \to 26.7\%$ while for $BR(B_c \to \tau\nu) < 10\%$ the p-value is increased from $0.3\% \to 14.1\%$. Hence, the latest data show that the impact of $BR(B_c \to \tau\nu)$ on the p-values becomes more crucial; therefore, an accurate measurement of $BR(B_c \to \tau\nu)$ will be helpful to clear the smog for the most favorable NP scenario.

Apart from the dependence of $BR(B_c \to \tau\nu)$, we also analyze the impact of N_{obs} on the parameters of NP scenarios. For this purpose, we compare the values of different parameters of Fits A, B, and C, which are listed in Table 3. The data of $R(J/\psi)$ and $R(\Lambda_c)$ directly affect the parametric space of NP scenarios as can be seen from the given values of different parameters in Table 3. These values show that the goodness of fit (the p-value) is decreased when we increase N_{obs}. For instance, the p-value of the most favorable scenario (C_S^L, C_S^R) at $BR(B_c \to \tau\nu) < 60\%$ is 71.5% for Fit A, is reduced up to 32.2% for Fit B, and is even further reduced for Fit C, where it is only 16.9%.

Interestingly, for Fit C, at $BR(B_c \to \tau\nu) < 10\%$, the most favorable scenario (C_S^L, C_S^R) becomes less favorable (p-value = 3.8) in comparison with some other NP scenarios, as we can see from the p-values given in Table 3. Although there is a large uncertainty in the experimental value of $R(J/\psi)$ and, similarly, the recent experimental measurement of $R(\Lambda_c)$ is under debate [2], the behavior in the analysis discussed above indicates that future data on different

Table 3. Fit results for 2D scenarios at 2 TeV, including all available data: best-fit points, $\chi^2_{\rm min}$, p-value, pull$_{\rm SM}$ are given. Columns 2–5 represent the results for different parameters: The first, second, and third rows represent Fits A, B, and C, respectively. The last eight columns show the predictions of different observables at the best-fit point with the σ deviation.

$\chi^2_{\rm SM} = (16.50, 19.76, 20.92)_{A,B,C}$, p-value $= (2.41, 1.38, 1.89)_{A,B,C} \times 10^{-3}$											
Scenarios	Best fit	$\chi^2_{\rm min}$	p-value %	pull$_{\rm SM}$	$R(D)$	$R(D^*)$	$R(J/\psi)$	$F_L(D^*)$	$P_\tau(D^*)$	$P_\tau(D)$	$R(\Lambda_c)$
$(C_V^L, C_S^L = -4C_T)$	(0.05,0.003)	2.42	29.8	3.75	0.336	0.284	0.289	0.462	−0.497	0.342	0.363
	(0.06,0.00)	5.20	15.7	3.82	−0.31σ	−0.08σ	−1.70σ	−1.54σ	−0.21σ		1.59σ
	(0.05,0.01)	7.86	9.68	3.61							
$(C_S^L, C_S^R)\vert_{60\%}$	(−0.65,−0.17),(−0.21,0.25)	0.67	71.5	3.98	0.339	0.285	0.287	0.524	−0.335	0.441	0.369
	(−0.65,−0.16),(−0.22,0.25)	3.49	32.2	4.03	−0.19σ	0σ	−1.71σ	−0.84σ	0.08σ		1.67σ
	(−0.63,−0.18),(−0.20,0.24)	6.43	16.9	3.81							
$(C_S^L, C_S^R)\vert_{30\%}$	(−0.58,−0.24),(−0.14,0.18)	1.57	45.6	3.86	0.341	0.275	0.278	0.508	−0.379	0.435	0.358
		4.53	20.9	3.90	−0.11σ	−0.83σ	−1.74σ	−1.02σ	0.001σ		1.52σ
		7.08	13.1	3.72							
$(C_S^L, C_S^R)\vert_{10\%}$	(−0.49,−0.34),(−0.03,0.09)	4.84	8.8	3.41	0.366	0.261	0.265	0.481	−0.451	0.502	0.370
		7.99	4.6	3.43	0.84σ	−2σ	−1.79σ	−1.33σ	−0.12σ		1.68σ
		10.11	3.8	3.29							
(C_V^L, C_S^R)	(0.05,0.01)	2.29	31.8	3.77	0.341	0.283	0.288	0.465	−0.493	0.350	0.364
		5.12	16.3	3.83	−0.11σ	−0.16σ	−1.70σ	−1.51σ	−0.20σ		1.61σ
		7.77	10	3.63							
$({\rm Re}[C_S^L = 4C_T], {\rm Im}[C_S^L = 4C_T])\vert_{60\%,30\%}$	(−0.04,±0.28)	2.64	26.7	3.72	0.337	0.285	0.288	0.455	−0.438	0.953	0.362
	(−0.04,±0.28)	5.47	14	3.55	−0.26σ	0σ	−1.70σ	−1.62σ	−0.10σ		1.58σ
	(−0.04,±0.27)	8.01	9.1	3.59							
$({\rm Re}[C_S^L = 4C_T], {\rm Im}[C_S^L = 4C_T])\vert_{10\%}$	(−0.02,±0.23)	3.91	14.1	3.55	0.333	0.274	0.276	0.457	−0.457	0.786	0.351
		6.92	7.44	3.58	−0.42σ	−0.91σ	−1.75σ	−1.59σ	−0.14σ		1.43σ
		9.0	6.1	3.45							

Table 4. 1σ and 2σ allowed parametric space by using the 60% branching ratio for 1D and 2D scenarios.

1D scenarios	1σ interval	2σ interval	2D scenarios	1σ interval	2σ interval
C_S^L	(0.03,0.11)	$(-0.004,0.13)$	$(C_V^L, C_S^L = -4C_T)$	$(0.04,0.07)\epsilon\ C_V^L$ $(-0.02,0.04)\epsilon\ C_S^L$	$(0.01,0.09)\epsilon\ C_V^L$ $(-0.05,0.05)\epsilon\ C_S^L$
C_S^R	(0.04,0.10)	(0.01,0.12)	(C_S^L, C_S^R)	$(-0.25,-0.16)\epsilon\ C_S^L$ $(0.20,0.27)\epsilon\ C_S^R$	$(-0.27,-0.14)\epsilon\ C_S^L$ $(0.18,0.28)\epsilon\ C_S^R$
C_V^L	(0.03,0.08)	(0.02,0.09)	(C_V^L, C_S^R)	$(0.03,0.07)\epsilon\ C_V^L$ $(-0.02,0.05)\epsilon\ C_S^R$	$(0.01,0.08)\epsilon\ C_V^L$ $(-0.05,0.07)\epsilon\ C_S^R$
$C_S^L = 4C_T$	$(-0.04,0.05)$	$(-0.08,0.08)$	$(\mathrm{Re}[C_S^L = 4C_T], \mathrm{Im}[C_S^L = 4C_T])$	$(-0.08,0.02)\epsilon\ RC_S^L$ $(-0.32,0.32)\epsilon\ \mathrm{Im}C_S^L$	$(-0.11,0.04)\epsilon\ RC_S^L$ $(-0.35,0.35)\epsilon\ \mathrm{Im}C_S^L$

Table 5. The best-fit point, $\chi^2_{\min}$, p-value, and pull$_{\mathrm{SM}}$ of 2D scenarios related to C_V^R at 2 TeV are given in columns 2–5. The first row represents Fit A, the second row represents Fit B, and the last row shows Fit C. The final seven columns show the predictions of different observables at the best-fit point with the sigma deviation.

$\chi^2_{\mathrm{SM}} = (16.50, 19.76, 20.92)_{A,B,C}$, p-value $= (2.41, 1.38, 1.89)_{A,B,C} \times 10^{-3}$											
Scenarios	Best fit	$\chi^2_{\min}$	p-value %	pull$_{\mathrm{SM}}$	$R(D)$	$R(D^*)$	$R(J/\psi)$	$F_L(D^*)$	$P_\tau(D^*)$	$P_\tau(D)$	$R(\Lambda_c)$
(C_V^L, C_V^R)	$(-0.89,-0.99.)$	2.37	30.5	3.76	0.332	0.286	0.291	0.464	-0.496	0.331	0.364
		5.17	15.9	3.82	-0.46σ	0.08σ	-1.69σ	-1.52σ	-0.21σ		1.61σ
		7.84	9.7	3.62							
(C_S^L, C_V^R)	$(0.09,-0.07)$	2.58	27.5	3.73	0.334	0.285	0.290	0.459	-0.522	0.553	0.360
		5.38	14.5	3.79	-0.38σ	$0.\sigma$	-1.69σ	-1.57σ	-0.26σ		1.55σ
		7.90	9.5	3.61							
(C_S^R, C_V^R)	$(0.08,-0.05)$	1.87	39.2	3.82	0.341	0.284	0.288	0.477	-0.469	0.532	0.363
		4.68	19.6	3.88	-0.11σ	-0.08σ	-1.70σ	-1.38σ	-0.16σ		1.59σ
		7.29	12.1	3.69							
$(C_V^R, C_S^L = 4C_T)$	$(-0.17,0.17)$	2.14	34.5	3.79	0.350	0.282	0.284	0.472	-0.568	0.763	0.364
		4.97	17.4	3.85	0.23σ	-0.25σ	-1.72σ	-1.43σ	-0.34σ		1.61σ
		8.58	10.7	3.65							

observables will also be valuable to decide which NP scenario is more suitable to explain the various anomalies.

The 1σ and 2σ intervals of these NP 1D and 2D scenarios are given in Table 4.

3.2.1. *Discussion about C_V^R-related scenarios.* In this section, we will discuss the possible scenarios associated with C_V^R, i.e. (C_V^L, C_V^R), (C_S^L, C_V^R), (C_S^R, C_V^R), and $(C_V^R, C_S^L = 4C_T)$, where the last one is related to the R_2 model [64]. The corresponding plots are shown in Fig. 3, with shaded brown, solid red, and dashed red contours representing Fits A, B, and C, respectively, at 2 TeV while the black contours are at 1 TeV. The purple region represents the LHC bounds at the 2σ level. It can be seen that these scenarios are independent of branching ratio constraints with the exception that the scenario (C_S^R, C_V^R) is slightly affected ($\approx 10\%$) by the branching ratio constraint. Moreover, the 1σ, 2σ allowed parametric space and the best-fit points of these scenarios are not significantly affected after including $R(J/\psi)$ (Fit B, solid red contour) and $R(\Lambda_c)$ (Fit C, dashed red contour) in the analysis. It is also noted that the parametric space for the scenario $(C_V^R, C_S^L = 4C_T)$ is impacted by the collider bounds, as seen by the purple region in Fig. 3d. The p-values and the other parameters for these scenarios are reported in Table 5. The trend and the variation in the values of χ^2, pull, and p-value with respect to N_{obs} show that the scenario (C_S^R, C_V^R) is most favorable among the other scenarios for Fit A while for Fit B the scenarios (C_S^R, C_V^R) and $(C_V^R, C_S^L = 4C_T)$ are both equally likely. However, to explore the NP

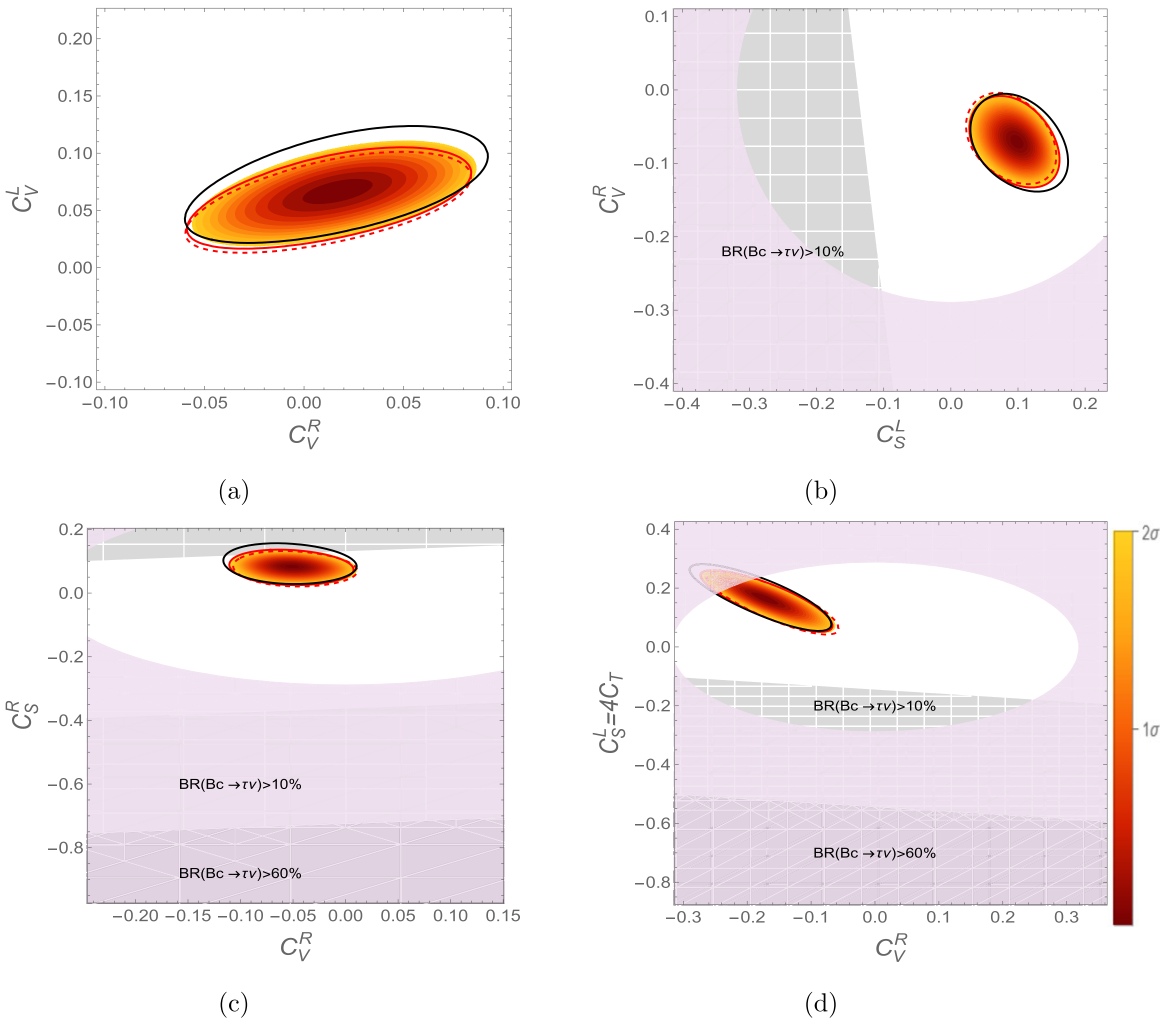

Fig. 3. Results of the fits for the 2D C_V^R scenarios (a) (C_V^L, C_V^R), (b) (C_S^L, C_V^R), (c) (C_V^R, C_S^R), and (d) $(C_V^R, C_S^L = 4C_T)$. The shaded contours represent Fit A, the solid contours represent Fit B, and the dashed contours represent Fit C. The gray portion represents the excluded regions by the 60% and 10% upper limits on the branching ratio $B_c \to \tau\nu$. The black contours show the allowed parametric space at 1 TeV. The purple region shows the collider bounds at the 2σ level.

Table 6. The current collider bounds of the NP WCs with 139 fb^{-1} based on the $\tau^{\pm}\nu$ search at $\mu = m_b$ [132]. The second row represents the values of these NP WCs at $\mu = 2$ TeV, where the values in parenthesis correspond to the HL-LHC 3000 fb^{-1} limit.

	C_V^L	C_V^R	C_S^L	C_S^R	C_T
$\mu = m_b$	0.30 (0.14)	0.32 (0.15)	0.55 (0.25)	0.55 (0.25)	0.15 (0.07)
$\mu = 2$ TeV	0.27 (0.13)	0.29 (0.14)	0.32 (0.15)	0.28 (0.13)	0.17 (0.08)

scenarios further, as mentioned in the previous section, the theoretical prediction of $R(J/\psi)$ and the experimental measurement of $R(\Lambda_c)$ require further precision.

3.3. *Impact of collider (LHC) bounds on 2D NP scenarios*

We would like to mention here that, at the LHC, the analysis of the $\tau+$ missing searches has given upper limits on the NP WCs [131,132] at the scale $\mu = m_b$; these are listed in Table 6. By using Eq. (3), the values of these NP WCs at $\mu = 2$ TeV are also given in Table 6, where the values in the parenthesis correspond to the HL-LHC 3000 fb^{-1} limit.

We have imposed these upper limits on the considered 2D NP scenarios. We have found that all the NP scenarios are within the limits coming from the analysis of the $\tau+$ missing searches shown by the purple region. However, the future prospects impose severe constraints on the scenarios: (Re[$C_S^L = 4C_T$], Im[$C_S^L = 4C_T$]), (C_S^L, C_S^R). We show these constraints by the blue shaded region in the plots of Figs. 2c and 2d. One can see that the lower portion of the scenario (Re[$C_S^L = 4C_T$], Im[$C_S^L = 4C_T$]) is completely excluded, while the best-fit point of the upper portion is excluded and the allowed region is drastically squeezed. Similarly, for the scenario (C_S^L, C_S^R), the best-fit points and large areas of both the upper and lower portions are also excluded.

4. Sum rule and correlation of observables

In this section, we calculate and analyze the correlation among different observables in 2D scenarios under consideration, but before that we want to validate the sum rule among the observables $R(D^{(*)})$ and $R(\Lambda_c)$ given in Refs. [1–3]. We can see that, by using Eqs. (4), (5), and (10), the sum rule reads

$$\frac{R(\Lambda_c)}{R_{\rm SM}(\Lambda_c)} = 0.276\frac{R(D)}{R_{\rm SM}(D)} + 0.724\frac{R(D^*)}{R_{\rm SM}(D^*)} + x_1, \tag{13}$$

where one can see that, even with the different analytical expressions of $R(D^{(*)})$, the coefficients of the first two terms on the right-hand side in the above equation are almost similar to those in Ref. [2]. The only change appears in the remainder x_1, which in our case becomes

$$x_1 = -\mathrm{Re}\left[\left(1 + C_V^L\right)\left(0.122\,(C_T)^* + 0.019\left(C_S^L\right)^* + 0.132\left(C_V^R\right)^*\right)\right]$$
$$+\mathrm{Re}\left[\left(C_V^R\right)^*\right]\left(0.018 C_S^R + 0.351 C_T\right). \tag{14}$$

The values of x_1 for 1D (2D) scenarios are 10^{-5} (10^{-3}) and the updated predicted value of $R(\Lambda_c)$ by using the latest data of $R(D^{(*)})$ [33] is

$$R(\Lambda_c) = R_{\rm SM}(\Lambda_c)\,(1.140 \pm 0.041)$$
$$= 0.369 \pm 0.013 \pm 0.005, \tag{15}$$

which is not significantly different from the numbers reported in Ref. [2]. This shows that the latest data of $R(D^{(*)})$ again confirm the validity of the above sum rule. In Eq. (15), the first and second errors come from the experimental and form factor uncertainties, respectively. However, the current experimentally measured value of $R(\Lambda_c)$ is larger than the predicted value by the sum rule as well as inconsistent with the $R(D^{(*)})$ data pattern and needs further experimental confirmation, as discussed in Ref. [2]. In addition, the latest predicted SM value of the observable $R(J/\psi) = 0.258 \pm 0.038$ [65] is smaller than its experimentally measured value, $0.71 \pm 0.17 \pm 0.18$ [2,18], which shows the same behavior as $R(\Lambda_c)$, i.e. a tau deficit, in contrast with the $R(D^{(*)})$ data. Therefore, it is also interesting to find out the sum rule for $R(J/\psi)$ in terms of $R(D^{(*)})$, which we have derived by using Eqs. (4), (5), and (9) as follows:

$$\frac{R(J/\psi)}{R_{\rm SM}(J/\psi)} = 0.006\frac{R(D)}{R_{\rm SM}(D)} + 0.994\frac{R(D^*)}{R_{\rm SM}(D^*)} + x_2, \tag{16}$$

where

$$x_2 = -\mathrm{Re}\left[\left(1 + C_V^L\right)\left(0.019C_S^{R^*} + 0.257C_T^* + 0.013C_V^{R^*} - 0.0004C_S^{L^*}\right)\right] + 0.006\left(\left|C_R^S\right|^2 + \left|C_L^S\right|^2\right)$$
$$+ 0.013\mathrm{Re}[C_S^L C_S^{R^*}] - 1.205\,|C_T|^2 - \mathrm{Re}[C_V^{R^*}]\left[0.018C_S^L - 0.0031C_T - 0.004C_S^R\right].$$

The remainder x_2 for this observable in the 1D (2D) scenario is 10^{-5} (10^{-3}). The predicted value of $R(J/\psi)$ by using the above sum rule is

$$R(J/\psi) = R_{\mathrm{SM}}(J/\psi)\,(1.119 \pm 0.046)$$
$$= 0.289 \pm 0.013 \pm 0.043. \tag{17}$$

One can see that both the SM value of $R(J/\psi)$ as well as its predicted value obtained by the sum rule using the updated data are smaller than its experimental value and follow a coherent pattern as in the $R(D^{(*)})$ case, i.e. a tau abundance in comparison with light leptons. However, in the case of $R(J/\psi)$, even though its tensor form factors are not precisely calculated yet, the theoretically predicted values are quite small compared to its experimental value with large uncertainties, $0.71 \pm 0.18 \pm 0.17$. We hope that in future this value will be further scrutinized at some ongoing and planned experiments.

It will be interesting to see how the updated data change the correlation among the $R(D^{(*)})$, $R(\Lambda_c)$, $F_L(D^*)$, and $P_\tau(D^{(*)})$ observables that are calculated in Ref. [1], and for that the updated and previous results are shown in Fig. 4 by using the 1σ parametric range of 2D scenarios. It is worth mentioning here that these correlations are significantly affected by considering the updated values of $R(D^{(*)})$ while the inclusion of $R(J/\psi)$ and the recently measured $R(\Lambda_c)$ data mildly affect the behavior of correlations. However, to see their effects explicitly, we also show the correlations of 1σ parametric space of Fit A (unfilled region) and Fit C (filled region) in Fig. 4. In addition, to see the effects by the scale of WCs on the correlations, we have also calculated these correlations at 1 TeV for Fit A, shown by the black curves. As mentioned in Section 3.2, the updated values of $R(D^{(*)})$ squeeze the parametric space of 2D scenarios significantly (see Fig. 2). Consequently, this shrinks and lowers the values of correlation regions among the observables $R(D^{(*)})$ and $R(\Lambda_c)$, which is closer to the SM values of these observables, as can be seen from the first four plots of Fig. 4. Similarly, the changes with the updated data for $R(D^{(*)})$ in the correlation regions among the observables $P_\tau(D^{(*)})$ and $F_L(D^*)$ are depicted in plots five to ten of Fig. 4. In addition, the correlations among $R(D^{(*)})$ and $R(J/\psi)$ are also shown in the last four plots of Fig. 4. On the other hand, for the scenarios related to C_V^R, the correlations among the observables by using the 1σ parametric space are plotted in Fig. 5.

Finally, from Eq. (12), the predicted values of the observables used in the fitting analysis are also calculated by using the 1σ parametric space of the 2D NP scenarios; we list them in Tables 3 and 5. It can be seen that the predicted values of $R(D^{(*)})$ and $P_\tau(D^*)$ show deviations smaller than 1σ, except for the scenarios ($\mathrm{Re}[C_S^L = 4C_T]$, $\mathrm{Im}[C_S^L = 4C_T]$) and ($C_S^L$, C_S^R) for the 10% branching ratio. However, the observables $R(J/\psi)$ and $F_L(D^*)$ exhibit 2σ deviation, except the scenario (C_S^L, C_S^R) for the 60% branching ratio for $R(J/\psi)$. Similarly, the predicted value of $R(\Lambda_c)$ is showing approximately 2σ deviation with respect to its experimentally measured numbers.

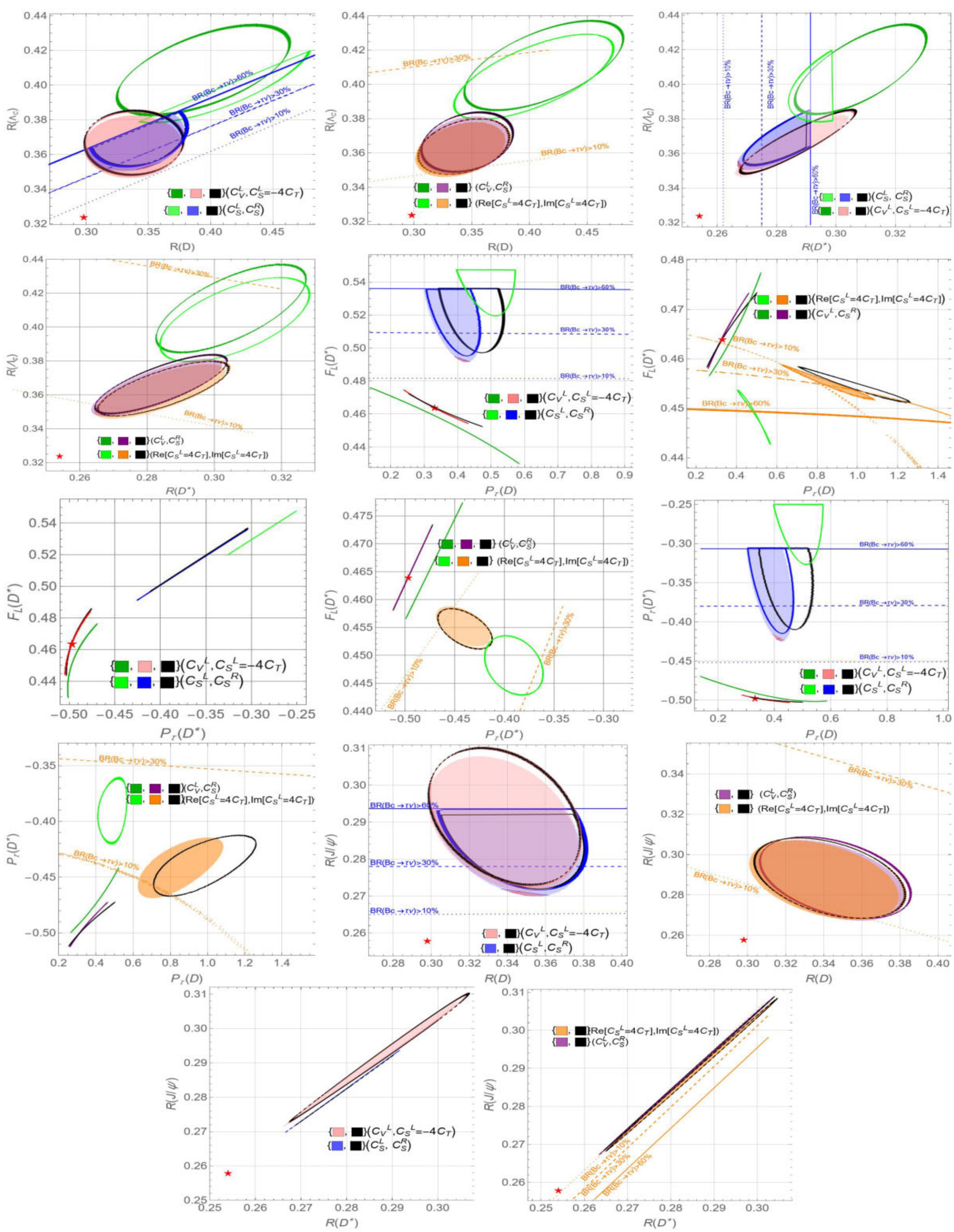

Fig. 4. Correlations plots for 1σ with $BR < 60\%$. The green (black) contours represent the plots of Ref. [1]; the filled (unfilled) contours represent Fit C (A). The solid, dashed, and dotted lines show $BR(60, 30, 10)\%$, respectively, while the red star represents SM. The meshed regions correspond to future constraints of the $\tau\nu$ analysis.

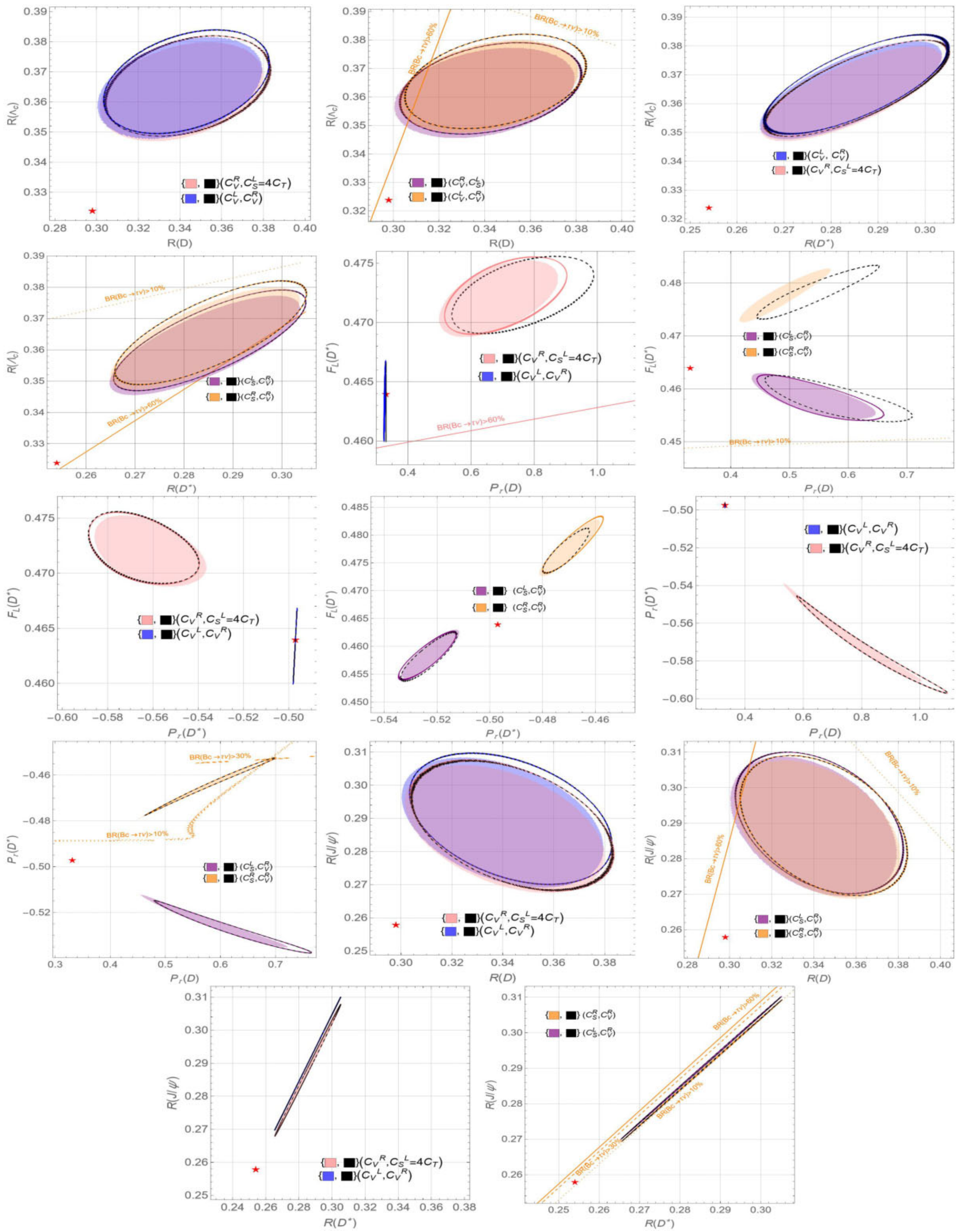

Fig. 5. The same as Fig. 4 but for C_V^R-related scenarios.

5. Sensitivity of angular observables to New Physics (NP)

For the NP point of view, it is important to mention here that the form factors are the main source of hadronic uncertainties, consequently generating errors in the theoretical predictions which may preclude the effects of NP. Therefore, we not only need to select those observables

Table 7. The SM and NP values of angular observables in the 2σ allowed parametric space in the full q^2 region for different 1D scenarios.

Observables	SM	C_S^L	C_S^R	C_V^L
A_3	-0.0170 ± 0.0001	-0.0171 ± 0.0001	-0.0169 ± 0.0001	-0.0170 ± 0.0001
A_4	0.0900 ± 0.0002	0.0907 ± 0.0006	0.0894 ± 0.0005	0.0900 ± 0.0002
A_5	-0.2059 ± 0.002	-0.2025 ± 0.003	-0.2091 ± 0.003	-0.2059 ± 0.002
A_{6s}	0.7985 ± 0.017	0.8043 ± 0.005	0.7924 ± 0.005	0.7985 ± 0.017
$R_{A,B}$	0.5725 ± 0.0009	0.5730 ± 0.0005	0.5719 ± 0.0001	0.5725 ± 0.0009
$R_{L,T}$	0.8611 ± 0.0036	0.8475 ± 0.011	0.8754 ± 0.011	0.8611 ± 0.0036
A_{FB}^T	-0.3302 ± 0.006	-0.3302 ± 0.006	-0.3302 ± 0.006	-0.3302 ± 0.006
A_{FB}^L	-0.0536 ± 0.004	-0.0603 ± 0.006	-0.0469 ± 0.005	-0.0536 ± 0.004
$F_L(D^*)$	0.4626 ± 0.001	0.4587 ± 0.004	0.4667 ± 0.003	0.4649 ± 0.001
C_F^L	-0.0691 ± 0.0009	-0.0697 ± 0.0006	-0.0686 ± 0.0005	-0.0691 ± 0.0009

that are sensitive to NP but also those for which variation in their values in the presence of NP may provide a discriminatory tool among the different NP scenarios.

To accomplish this, we have considered the lepton forward–backward asymmetry (A_{FB}^{ℓ}), the forward–backward asymmetry of the transversely polarized D^* meson ($A_{FB}^{T,L}$), the longitudinal polarization fraction of the D^* meson ($F_L(D^*)$), the ratios ($R_{A,B}$, $R_{L,T}$), and the angular asymmetries (A_3, A_4, A_5, A_{6s}) for the decay channel $B \to D^*\tau\nu_\tau$, which are relatively clean and also sensitive to the NP. Therefore, the variations in their values in the presence of the 1D and 2D NP scenarios under consideration could be used to discriminate these NP scenarios. These CP-even angular observables are discussed in detail in the literature and their analytical expressions in terms of angular coefficients, I_i, can be found in Refs. [44,72,81]. Furthermore, in the current study, we rely on the form factors that are calculated in Refs. [44,81] and the observables mentioned above have been presented with their theoretical uncertainties.

To see the sensitivity of these angular observables to NP, we have plotted them against the square of transverse momentum, q^2, in Figs. 6 and 8 for 1D and 2D NP scenarios, respectively. In these figures, the black (gray) band shows the SM values of these observables where the width corresponds to the uncertainty in the values due to the form factors. The color bands represent their values in the presence of NP. For the NP dependence of these observables, we have used the central values of the form factors and the widths of the light and dark color bands show the uncertainty due to 1σ and 2σ intervals in the NP WCs at 2 TeV, respectively. The effects of different 1D and 2D NP scenarios on the above-mentioned angular observables are discussed in the following sections. In addition, to see the direct influence of the scenarios on the observables, we have also found the expressions for I_i in terms of NP WCs, $C_i^{L(R)}$, after integrating q^2; these are given in Appendix A.

One can immediately see that the expressions of coefficients I_i in terms of NP WCs make the study of NP with different angular observables quite trivial. Therefore, by using these expressions for I_i, we have calculated the variations in the amplitudes of different angular observables in the presence of NP, shown by the bar plots in Figs. 7 and 9 for 1D and 2D NP scenarios, respectively. The corresponding SM predictions and values at different scenarios are also listed in Tables 7 and 8, respectively.

As we mentioned in Section 3, for the scenarios (C_V^L, $C_S^L = -4C_T$), (C_V^L, C_S^R) the allowed parametric space of NP does not significantly change with the number of observables and

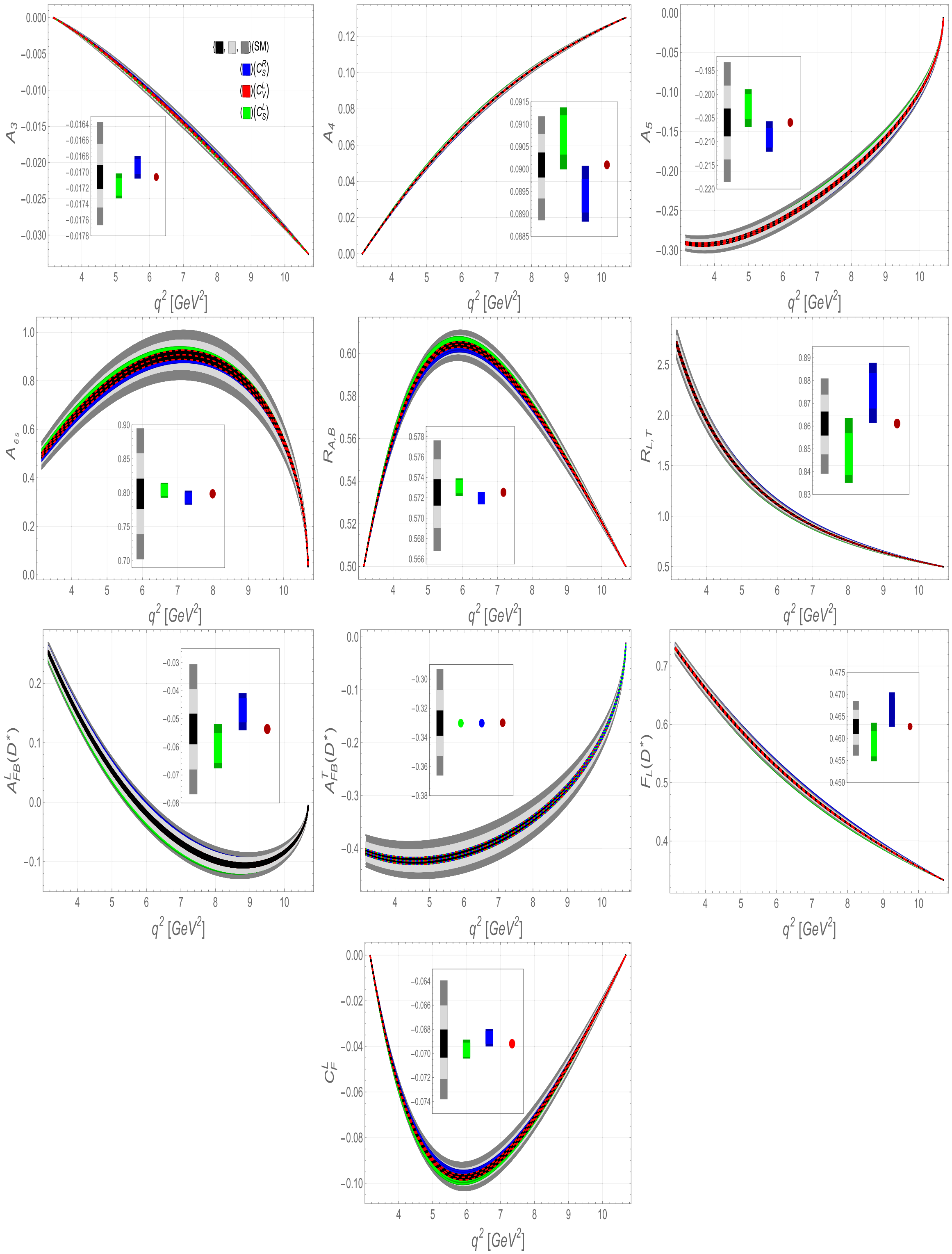

Fig. 6. A_{3-5}, A_{6s}, $R_{A,B}$, $R_{L,T}$, $A_{FB}^{L,T}(D^*)$, $F_L(D^*)$, and C_F^L for $\bar{B} \to D^*\tau\bar{\nu}$ are shown for allowed values of NP couplings for 1D scenarios as a function of q^2. The black, light gray, and gray portions represent the variation in the SM value due to the uncertainties of the form factors and 5% and 10% statistical uncertainties of future experiments, respectively, while the light and dark color bands reflect the 1σ and $2\,\sigma$ ranges of NP scenarios.

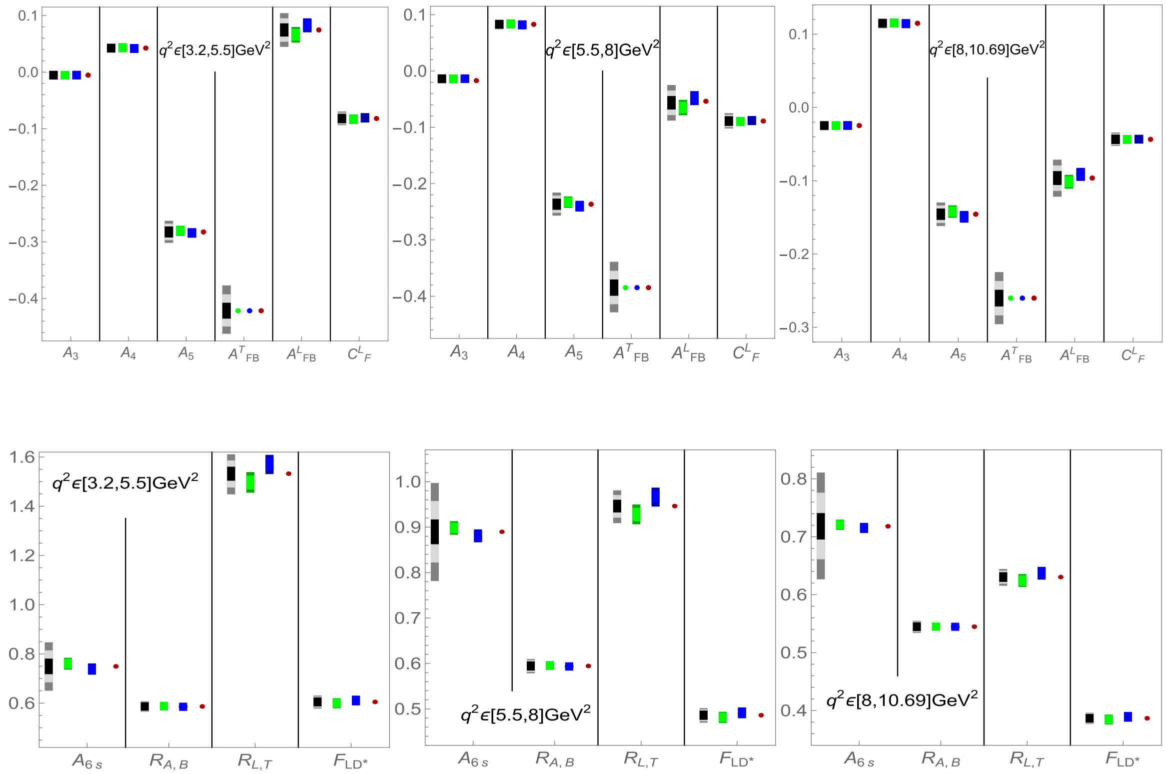

Fig. 7. Bar plots of A_{3-5}, A_{6s}, $R_{A,B}$, $R_{L,T}$, $A_{FB}^{L,T}(D^*)$, $F_L(D^*)$, and C_F^L for $\bar{B} \to D^*\tau\bar{\nu}$ are shown. The bar plots in the first and second rows show the numerical values in different q^2 bins. The black bar shows the SM variation of angular observables and the color bars show the variation in the numerical values in the different NP scenarios.

Table 8. The SM and NP values of angular observables in the 2σ allowed parametric space in the full q^2 region for different 2D scenarios.

Observables	SM	$(C_V^L, C_S^L = -4C_T)$	(C_S^L, C_S^R)	(C_V^L, C_S^L)	$(\mathrm{Re}[C_S^L = 4C_T], \mathrm{Im}[C_S^L = 4C_T])$
A_3	-0.0170 ± 0.0001	-0.0170 ± 0.0001	-0.0162 ± 0.0001	-0.0001 ± 0.0001	-0.0148 ± 0.003
A_4	0.0900 ± 0.0002	0.0890 ± 0.007	0.0856 ± 0.0002	0.900 ± 0.0005	0.0828 ± 0.009
A_5	-0.2059 ± 0.002	-0.2037 ± 0.009	-0.2233 ± 0.0006	-0.2063 ± 0.003	-0.1935 ± 0.007
A_{6s}	0.7985 ± 0.017	0.7861 ± 0.04	0.7591 ± 0.002	0.7977 ± 0.006	0.7240 ± 0.011
$R_{A,B}$	0.5725 ± 0.001	0.5717 ± 0.008	0.5688 ± 0.0009	0.5724 ± 0.0005	0.5726 ± 0.0009
$R_{L,T}$	0.8611 ± 0.0036	0.8559 ± 0.002	0.9760 ± 0.003	0.8630 ± 0.011	0.8257 ± 0.011
A_{FB}^T	-0.3302 ± 0.006	-0.3242 ± 0.033	-0.3302 ± 0.006	-0.3302 ± 0.006	-0.2855 ± 0.044
A_{FB}^L	-0.0536 ± 0.004	-0.0518 ± 0.008	-0.0149 ± 0.008	-0.0527 ± 0.006	-0.0407 ± 0.03
$F_L(D^*)$	0.4626 ± 0.001	0.4611 ± 0.009	0.4891 ± 0.0001	0.4632 ± 0.003	0.4522 ± 0.002
C_F^L	-0.0691 ± 0.0009	-0.0684 ± 0.005	-0.0657 ± 0.0001	-0.0691 ± 0.0004	-0.0692 ± 0.008

the branching ratio constraints, while the allowed parametric space of the scenarios ($\mathrm{Re}[C_S^L = 4C_T]$, $\mathrm{Im}[C_S^L = 4C_T]$), (C_S^L, C_S^R) is affected only by the branching ratio constraints. It is worth mentioning here that we have found that the allowed 1σ and 2σ parametric spaces for Fits A, B, and C are almost the same. However, to see the impact of NP effects on the numerical values of angular observables, we use the 1σ and 2σ parametric space with the 60% branching ratio as given in Table 4 with the constraints coming from LHC bounds on the 2D scenarios, $(C_V^L, C_S^L = -4C_T)$, (C_V^L, C_S^R), which are discussed in Section 6.

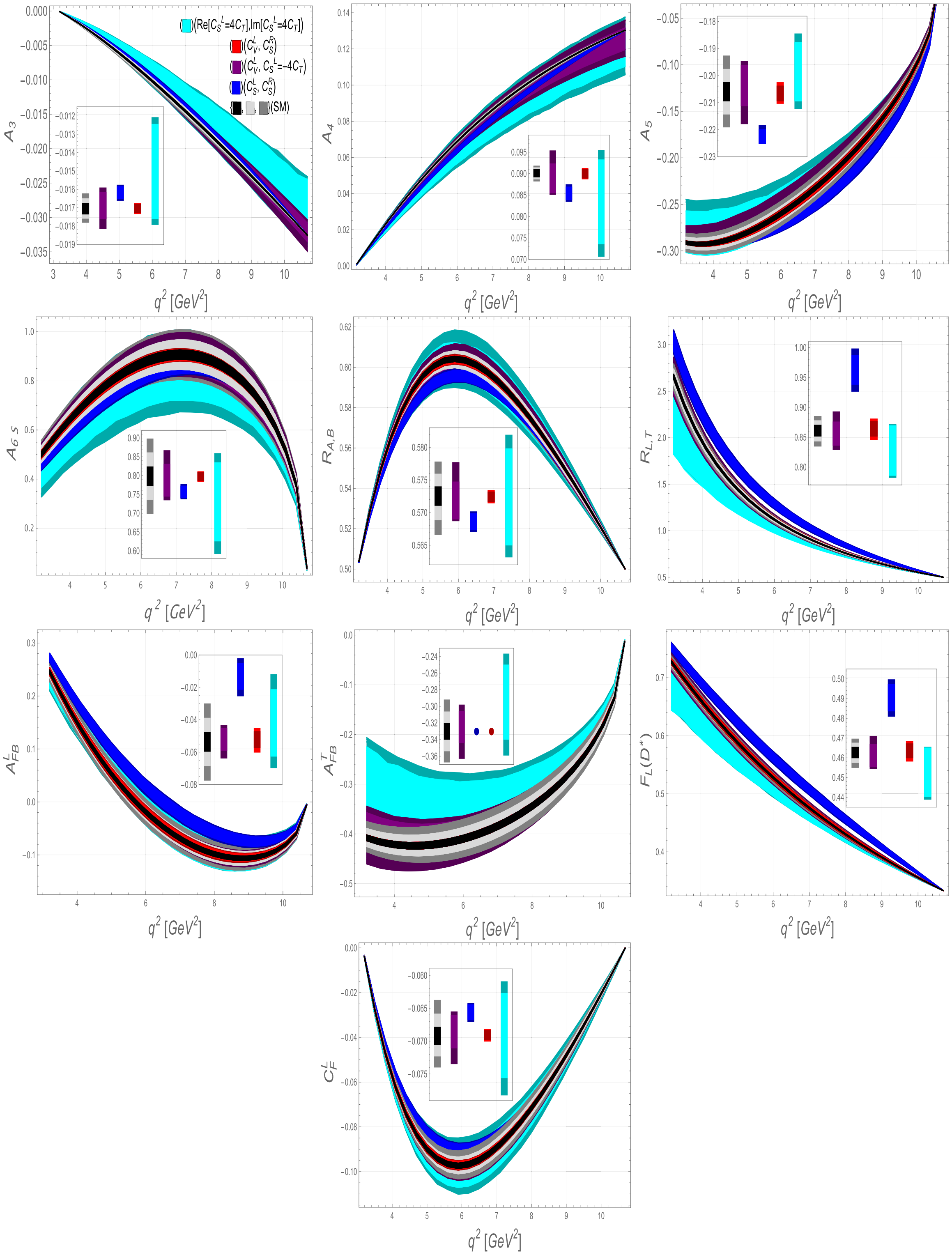

Fig. 8. The same as Fig. 6 but for 2D scenarios.

5.1. *Effects of 1D scenarios on observables*

The sensitivity of different angular observables by taking one of the NP WCs, $C_i^{(L,R)}$, is set to be nonzero and is plotted in Fig. 6. In these plots, we took the numerical values of the NP WCs after imposing the current prospects of the collider bounds. As for scenario $C_S^L = 4C_T$,

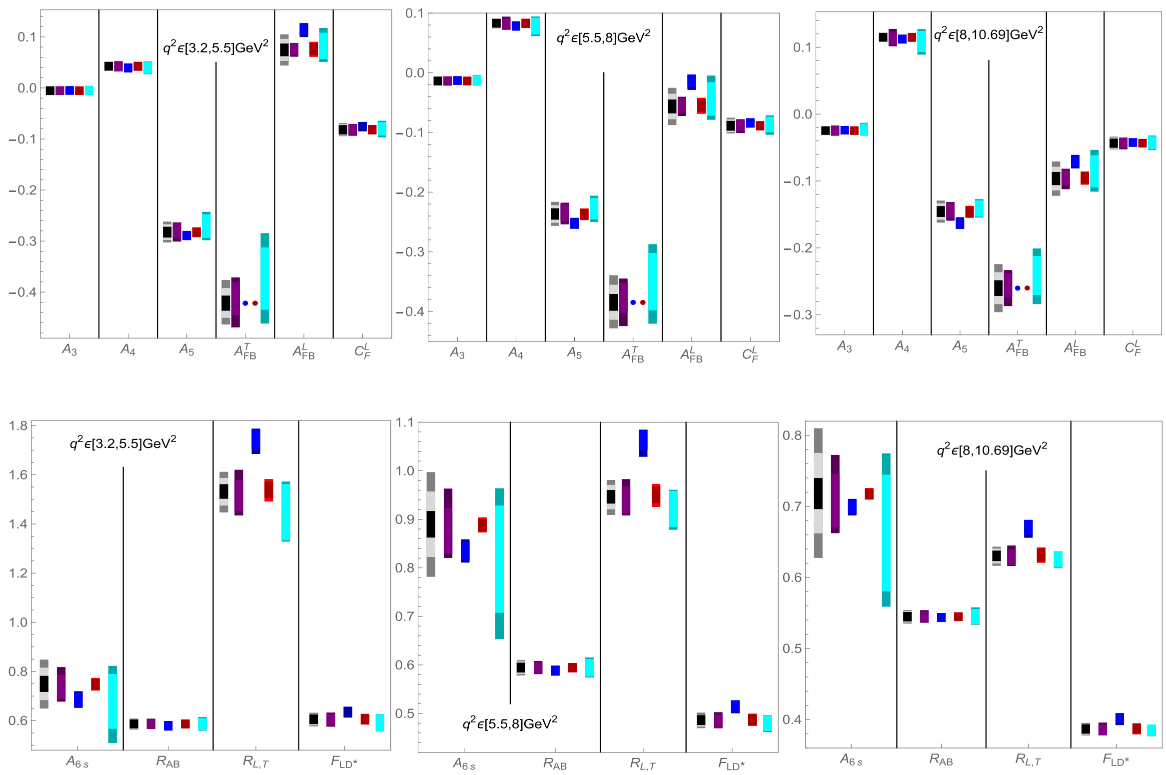

Fig. 9. The same as Fig. 7 but for 2D scenarios.

the pull$_{\text{SM}}$ value is too small; therefore, this scenario is not included in the q^2 analysis. In this figure, the black, light gray, and gray portions represent the variation in the SM value due to the uncertainties of the form factors and 5% and 10% statistical uncertainties of future experiments, respectively. One can notice that the 1D scenarios are almost precluded by these uncertainties. However, if the future experimental uncertainties are limited to 5% then the values of the observables A_4, $R_{L,T}$, $F_L(D^*)$ exceed their SM values, which may help to distinguish the 1D NP scenarios. Therefore, binwise precise measurements of the observables are also important to probe the NP and to distinguish between different NP scenarios. For this purpose, we have also calculated the full variation in the values of observables by using the 1σ to 2σ ranges of WCs of 1D scenarios after integrating the full region and different q^2 bins; these are shown by the bar plots in Fig. 7. The SM values and the values in the different 1D NP scenarios of the angular observables in the full q^2 region are also given in Table 7.

5.2. *Effects of 2D scenarios on observables*

In order to keep the analysis consistent, we imposed the current collider bounds, as seen in Fig. 8, to depict the angular observables. It is clear from the figure that the observables are not sensitive to the scenario (C_V^L, C_S^R) (red band), whereas they are influenced by the other 2D scenarios; in particular, $(\text{Re}[C_S^L = 4C_T], \text{Im}[C_S^L = 4C_T])$ has a large effect (cyan band) on the values of the angular observables. One can also see that the effects of NP scenarios, $(\text{Re}[C_S^L = 4C_T], \text{Im}[C_S^L = 4C_T])$ (cyan band), $(C_V^L, C_S^L = -4C_T)$ (purple band), are increased (decreased) when the q^2 value increases for A_3, A_4 (A_5, $R_{L,T}$, $F_L(D^*)$, and A_{FB}^T), whereas the observables A_{6S}, $R_{A,B}$, A_{FB}^L, and C_F^L are largely affected in the middle of the q^2 region. Therefore, we have not only plotted the variations in the amplitudes due to the 2D NP scenarios when integrated over the whole q^2 region but also in different q^2 bins; these are shown in Fig. 9. Moreover, the scalar coupling scenario (C_S^L, C_S^R) (blue band) only increases (decreases) the values of A_3, $R_{L,T}$, A_{FB}^L, $F_L(D^*)$, C_L^F (A_4, A_5, A_{6S}, $R_{A,B}$, A_{FB}^T) with respect to their SM values throughout the q^2 region. On the other hand, the scenarios (Re[$C_S^L = 4C_T$], Im[$C_S^L = 4C_T$]), (C_V^L, $C_S^L = -4C_T$) raise and lower the values of these observables from their SM predictions throughout the q^2 region. In addition, to see the total variation in the magnitude of the numerical values of different angular observables, we have also calculated their numerical values by using the 2σ parametric space of 2D scenarios and listed them in Table 8 along with their SM results.

6. Summary and conclusions

In the current study, we have first checked the impact of recently measured data of $R(D^{(*)})$ and $R(\Lambda_c)$ [33] on different 1D and 2D NP scenarios that are considered in Refs. [1–3]. In addition, we have also included in the analysis $R(J/\psi)$ data that were not considered in previous studies, and found that their influence on the best-fit point and the parametric space is not significantly large. We have also validated (in light of recent data) the robustness of the sum rule of $R(\Lambda_c)$ and, similarly, found the sum rule for $R(J/\psi)$ in terms of $R(D^{(*)})$. From this sum rule, we have also predicted the value of $R(J/\psi)$, which is smaller than its experimental value. Instead, the form factors of $R(J/\psi)$ are not precisely calculated but the difference between the experimental and theoretical values is quite large; therefore, to see the agility of the sum rule of $R(J/\psi)$ and NP, it is mandatory to confirm the $R(J/\psi)$ value from further experiments. Furthermore, we have also modified the correlation among the different observables given in Ref. [1] according to the recent development in the data and also shown some more interesting correlations among observables. Finally, to discriminate the NP scenarios from each other, we have plotted the different angular observables against q^2, by using the 1σ and 2σ parametric space of NP scenarios with the constraints of collider bounds. Further to see the influence of NP on the amplitude of the angular observables, we have also calculated their numerical values in different q^2 bins and shown them through bar plots. We have found that angular observables are not only sensitive to NP but also very useful to find out the precise values of possible NP couplings, consequently helping us in discriminating various NP scenarios.

Acknowledgments

The authors would like to express their sincere gratitude to Prof. Monika Blanke et al. and Dr. Nestor Quintero for valuable feedback on our queries during the course of this study, which enabled us to understand their work.

Funding

Open Access funding: SCOAP^3.

A. Expressions for I_i

As mentioned in Section 5, the expressions for I_i can be found in Refs. [44,72,81]. However, I_i after integrating over q^2 can be expressed in terms of $C_i^{L(R)}$ as follows. These expressions are given as

$$I_1^s = 6.02 \times 10^{-15}\Big\{|1 + C_V^L|^2 + |C_V^R|^2 - 1.63\mathrm{Re}\Big[\left(1 + C_V^L\right)\left(C_V^R\right)^*\Big] - 4.68\mathrm{Re}\left[\left(1 + C_V^L\right)\left(C_T\right)^*\right]$$

$$+ 16.2|C_T|^2 + 7.6\mathrm{Re}\left[\left(C_V^R\right)\left(C_T\right)^*\right]\Big\},$$

$$I_1^c = 9.05 \times 10^{-15}\left\{\left|1 + C_V^L - C_V^R\right|^2 + 0.08\left|1 + C_S^R - C_S^L\right|^2 - 0.242\mathrm{Re}\left[\left(1 + C_V^L - C_V^R\right)\left(C_S^L\right)^*\right]\right.$$

$$\left. + 0.242\mathrm{Re}\left[\left(1 + C_V^L - C_V^R\right)\left(C_S^R\right)^*\right] - 4.07\mathrm{Re}\left[\left(1 + C_V^L(C_V^R\right)\left(C_S^R\right)^*\right]\right\} + 6.24\left|C_T\right|^2$$

$$I_2^c = -5.43 \times 10^{-15}\left\{\left|1 + C_V^L - C_V^R\right|^2 + 8.31\left|C_T\right|^2\right\},$$

$$I_2^s = 9.99 \times 10^{-16}\left\{\left|1 + C_V^L - C_V^R\right|^2 - 21.7\left|C_T\right|^2\right\},$$

$$I_3 = 1.67 \times 10^{-15}\left\{-\left|1 + C_V^L - C_V^R\right|^2 - 12.5\left|C_T\right|^2\right\},$$

$$I_4 = 2.23 \times 10^{-15}\left\{-\left|1 + C_V^L - C_V^R\right|^2 - 12\left|C_T\right|^2\right\},$$

$$I_5 = 4.49 \times 10^{-15}\Big\{\left|1 + C_V^L - C_V^R\right|^2 - 5.75\left|C_T\right|^2 + 2.04\left[\left|C_S^L - C_S^R\right| C_T^*\right]$$

$$- 1.26\mathrm{Re}\left[\left(C_V^R\right)\left(C_T\right)^*\right]\Big\},$$

$$I_6^c = 5.44 \times 10^{-15}\Big\{\left|1 + C_V^L - C_V^R\right|^2 - 0.67\mathrm{Re}\left[\left(1 + C_V^L - C_V^R\right)\left(C_S^{L*}\right)\right]$$

$$+ 0.67\mathrm{Re}\left[\left(1 + C_V^L - C_V^R\right)\left(C_S^{R*}\right)\right] - 3.76\mathrm{Re}\left[\left(1 + C_V^L\right)\left(C_T\right)^*\right] + \left[\left|C_S^L - C_S^R\right| C_T^*\right]\Big\},$$

$$I_6^s = -3.85 \times 10^{-15}\Big\{\left|1 + C_V^L\right|^2 + \left|C_V^R\right|^2 - 17.5\left|C_T\right|^2 - 2.59\mathrm{Re}\left[\left(1 + C_V^L\right)\left(C_T\right)^*\right]$$

$$- 8.54\mathrm{Re}\left[\left(C_V^R\right)\left(C_T\right)\right]\Big\}.$$

References

[1] M. Blanke, A. Crivellin, S. de Boer, T. Kitahara, M. Moscati, U. Nierste, and I. Nisandzic, Phys. Rev. D **99**, 075006 (2019) [arXiv:1811.09603 [hep-ph]] [Search inSPIRE].

[2] M. Fedele, M. Blanke, A. Crivellin, S. Iguro, T. Kitahara, U. Nierste, and R. Watanabe Phys. Rev. D **107**, 055005 (2023)[arXiv:2211.14172 [hep-ph]][Search inSPIRE]. .

[3] M. Blanke, A. Crivellin, T. Kitahara, M. Moscati, U. Nierste, and I. Nisandzic, Phys. Rev. D **100**, 035035 (2019) [arXiv:1905.08253 [hep-ph]] [Search inSPIRE].

[4] R. Dutta, A. Bhol, and A. K. Giri, Phys. Rev. D **88**, 114023 (2013) [arXiv:1307.6653 [hep-ph]] [Search inSPIRE].

[5] R. Dutta and A. Bhol, Phys. Rev. D **96**, 076001 (2017) [arXiv:1701.08598 [hep-ph]] [Search inSPIRE].

[6] R. Dutta, arXiv:1710.00351 [hep-ph][Search inSPIRE].

[7] R. Dutta and N. Rajeev, Phys. Rev. D **97**, 095045 (2018) [arXiv:1803.03038 [hep-ph]] [Search inSPIRE].

[8] A. Azatov, D. Barducci, D. Ghosh, D. Marzocca, and L. Ubaldi, J. High Energy Phys. **1810**, 092 (2018) [arXiv:1807.10745 [hep-ph]] [Search inSPIRE].

[9] J. Heeck and D. Teresi, J. High Energy Phys. **1812**, 103 (2018) [arXiv:1808.07492 [hep-ph]] [Search inSPIRE].
[10] X. Qiang Li, Y. D. Yang, and X. Zhang, J. High Energy Phys. **1608**, 054 (2016) [arXiv:1605.09308 [hep-ph]] [Search inSPIRE].
[11] R. Aaij et al. Phys. Rev. Lett. **113**, 151601 (2014) [arXiv:1406.6482 [hep-ex]] [Search inSPIRE].
[12] Y. Sakaki, M. Tanaka, A. Tayduganov, and R. Watanabe, Phys. Rev. D **88**, 094012 (2013) [arXiv:1309.0301 [hep-ph]] [Search inSPIRE].
[13] I. Caprini, L. Lellouch, and M. Neubert, Nucl. Phys. B **530**, 153 (1998) [arXiv:hep-ph/9712417] [Search inSPIRE].
[14] J. A. Bailey et al. Phys. Rev. D **89**, 114504 (2014) [arXiv:1403.0635 [hep-lat]] [Search inSPIRE].
[15] Z. Ligeti, M. Papucci, and D. J. Robinson, J. High Energy Phys. **1701**, 083 (2017) [arXiv:1610.02045 [hep-ph]] [Search inSPIRE].
[16] A. Abdesselam et al.[arXiv:1903.03102 [hep-ex]] [Search inSPIRE].
[17] A. Abdesselam et al.[arXiv:1904.08794 [hep-ex]][Search inSPIRE].
[18] R. Aaij et al., Phys. Rev. Lett. **120**, 121801 (2018) [arXiv:1711.05623 [hep-ex]] [Search inSPIRE].
[19] C. W. Murphay and A. Soni,, Phys. Rev. D **98,** 094026 (2018)[arXiv:1808.05392 [hep-ph]][Search inSPIRE].
[20] S. Kamali, A. Rashed, and A. Datta, Phys. Rev. D **97**, 095034 (2018) [arXiv:1801.08259 [hep-ph]] [Search inSPIRE].
[21] Y. Grossman and Z. Ligeti, Phys. Lett. B **332**, 373 (1994) [arXiv:hep-ph/9403376] [Search inSPIRE].
[22] P. Colangelo and F. De Fazio, Phys. Rev. D **95**, 011701 (2017) [arXiv:1611.07387 [hep-ph]] [Search inSPIRE].
[23] R. Aaij et al., Phys. Rev. Lett. **128** 191803 (2022).
[24] W. Detmold, C. Lehner, and S. Meinel, Phys. Rev. D **92** 034503 (2015) [arXiv:1503.01421 [hep-lat]] [Search inSPIRE].
[25] J. P. Lees et al., Phys. Rev. Lett. **109**, 101802 (2012) [arXiv:1205.5442 [hep-ex]] [Search inSPIRE].
[26] J. P. Lees et al., Phys. Rev. D **88**, 072012 (2013) [arXiv:1303.0571 [hep-ex]] [Search inSPIRE].
[27] M. Huschle et al., Phys. Rev. D **92**, 072014 (2015) [arXiv:1507.03233 [hep-ex]] [Search inSPIRE].
[29] A. Abdesselam, et al. ICHEP (2016) [arXiv:1608.06391 [hep-ex]][Search inSPIRE].
[28] Y. Sato et al., Phys. Rev. D **94**, 072007 (2016) [arXiv:1607.07923 [hep-ex]] [Search inSPIRE].
[30] G. Caria et al., Phys. Rev. Lett. **124**, 161803 (2020) [arXiv:1910.05864] [Search inSPIRE].
[31] R. Aaij et al., Phys. Rev. Lett. **115**, 111803 (2015) [arXiv:1506.08614 [hep-ex]] [Search inSPIRE].
[32] R. Aaij et al., Phys. Rev. Lett. **120,** 171802 (2018) [arXiv:1708.08856 [hep-ex]][Search inSPIRE].
[33] https://hflav-eos.web.cern.ch/hflav-eos/semi/moriond24/html/RDsDsstar/RDRDs.html. Preliminary average of $R(D)$ and $R(D*)$ for Moriond on 27th March, 2024 .
[34] S. Fajfer, J. F. Kamenik, and I. Nisandzic, Phys. Rev. D **85**, 094025 (2012) [arXiv:1203.2654 [hep-ph]] [Search inSPIRE].
[35] J. F. Kamenik and F. Mescia, Phys. Rev. D **78**, 014003 (2008) [arXiv:0802.3790 [hep-ph]] [Search inSPIRE].
[36] Y. Amhis et al., Eur. Phys. J. C **77**, 895 (2017) [arXiv:1612.07233 [hep-ph]] [Search inSPIRE].
[37] J. A. Bailey et al., Phys. Rev. Lett. **109**, 071802 (2012) [arXiv:1206.4992 [hep-ph]] [Search inSPIRE].
[38] J. A. Bailey et al., Phys. Rev. D **92**, 034506 (2015) [arXiv:1503.07237 [hep-ph]] [Search inSPIRE].
[39] S. Aoki et al., Eur. Phys. J. C **77**, 112 (2017) [arXiv:1607.00299 [hep-lat]] [Search inSPIRE].
[40] S. Hirose et al., Phys. Rev. Lett. **118**, 211801 (2017) [arXiv:1612.00529 [hep-ex]] [Search inSPIRE].
[41] S. Hirose et al., Phys. Rev. D **97**, 012004 (2018) [arXiv:1709.00529 [hep-ex]] [Search inSPIRE].
[42] M. Tanaka and R. Watanabe, Phys. Rev. D **87**, 034028 (2013) [arXiv:1212.1878 [hep-ph]] [Search inSPIRE].
[43] P. Asadi, M. R. Buckley, and D. Shih,, Phys. Rev. D **99**, 035015 (2019)[arXiv:1810.06597 [hep-ph]][Search inSPIRE].
[44] A. K. Alok, D. Kumar, S. Kumbhakar, and S. U. Sankar, Phys. Rev. D **95**, 115038 (2017) [arXiv:1606.03164 [hep-ph]] [Search inSPIRE].
[45] M. Tanaka and R. Watanabe, Phys. Rev. D **82**, 034027 (2010) [arXiv:1005.4306 [hep-ph]] [Search inSPIRE].

[46] Presentation by M. Fontana, on behalf of LHCb Collaboration, [talk slide]
[47] R. Watanabe, Phys. Lett. B **776**, 5 (2018) [arXiv:1709.08644 [hep-ph]] [Search inSPIRE].
[48] B. Chauhan and B. Kindra, arXiv:1709.09989 [hep-ph][Search inSPIRE].
[49] T. D. Cohen, H. Lamm, and R. F. Lebed, J. High Energy Phys. **1809**, 168 (2018) [arXiv:1807.02730 [hep-ph]] [Search inSPIRE].
[50] C. T. Tran, M. A. Ivanov, J. G. Korner, and P. Santorelli, Phys. Rev. D **97**, 054014 (2018) [arXiv:1801.06927 [hep-ph]] [Search inSPIRE].
[51] A. Issadykov and M. A. Ivanov, Phys. Part. Nucl. Lett. **20**, 355 (2023) [arXiv:2307.05013 [hep-ph]] [Search inSPIRE].
[52] K. Azizi, Y. Sarac, and H. Sundu, Phys. Rev. D **99**, 113004 (2019) [arXiv:1904.08267 [hep-ph]] [Search inSPIRE].
[53] K. Adamczyk, Talk at 10th International Workshop on the CKM unitarity Triangle, Heidelberg, 17-21 Sep. 2018 (2018).
[54] A. Celis, M. Jung, X. Q. Li, and A. Pich, Phys. Lett. B **771**, 168 (2017) [arXiv:1612.07757 [hep-ph]] [Search inSPIRE].
[55] P. Asadi, M. R. Buckley, and D. Shih, J. High Energy Phys. **1809**, 010 (2018)[arXiv:1804.04135 [hep-ph]] [Search inSPIRE].
[56] S. Iguro, T. Kitahara, Y. Omura, R. Watanabe, and K. Yamamoto, J. High Energy Phys. **1902**, 194 (2019) [arXiv:1811.08899 [hep-ph]] [Search inSPIRE].
[57] R. Alonso, B. Grinstein, and J. Martin Camalich, Phys. Rev. Lett. **118**, 081802 (2017) [arXiv:1611.06676 [hep-ph]] [Search inSPIRE].
[58] A. G. Akeroyd and C. H. Chen, Phys. Rev. D **96**, 075011 (2017) [arXiv:1708.04072 [hep-ph]] [Search inSPIRE].
[59] S. S. Gershtein, V. V. Kiselev, A. K. Likhoded, and A. V. Tkabladze, Phys. Usp. **38**, 1 (1995).
[60] I. I. Y. Bigi, Phys. Lett. B **371**, 105 (1996)[arXiv:hep-ph/9510325] [Search inSPIRE].
[61] M. Beneke and G. Buchalla, Phys. Rev. D **53**, 4991 (1996) [arXiv:hep-ph/9601249] [Search inSPIRE].
[62] C.-H. Chang, S.-L. Chen, T.-F. Feng, and X.-Q. Li, Phys. Rev. D **64**, 014003 (2001) [arXiv:hep-ph/0007162] [Search inSPIRE].
[63] V. V. Kiselev, A. E. Kovalsky, and A. K. Likhoded, Nucl. Phys. B **585**, 353 (2000) [arXiv:hep-ph/0002127] [Search inSPIRE].
[64] S. Iguro, T. Kitahara, and R. Watanabe[arXiv:2210.10751 [hep-ph]][Search inSPIRE].
[65] LATTICE-HPQCD Collaboration, Phys. Rev. Lett. **125**, 222003 (2020) [arXiv:2007.06956] [Search inSPIRE].
[66] HPQCD Collaboration, Phys. Rev. D **102**, 094518 (2020)[arXiv:2007.06957] [Search inSPIRE].
[67] LHCb Collaboration, Phys. Rev. Lett. **128**, 191803 (2022) [arXiv:2201.03497] [Search inSPIRE].
[68] S. Kamali, Int. J. Mod. Phys. A **34**, 1950036 (2019) [arXiv:1811.07393 [hep-ph]] [Search inSPIRE].
[69] R. X. Shi, L. S. Geng, B. Grinstein, S. Jager, and J. Martin Camalich, J. High Energy Phys. **1912**, 065 (2019) [arXiv:1905.08498 [hep-ph]] [Search inSPIRE].
[70] T. Bhattacharya, V. Cirigliano, S. D. Cohen, A. Filipuzzi, M. G. Alonso, M. L. Graesser, R. Gupta,, and H.W. Lin, Phys. Rev. D **85**, 054512 (2012) [arXiv:1110.6448 [hep-ph]] [Search inSPIRE].
[71] M. Antonelli et al. [FlaviaNet Working Group on Kaon Decays Collaboration], Nucl. Phys. Proc. Suppl. 181–182,83-88 (2008) [arXiv:0801.1817 [hep-ph][[Search inSPIRE].
[72] B. Damir, M. Fedele, I. Nisandzic, and A. Tayduganov[arXiv:1907.02257 [hep-ph]][Search inSPIRE].
[73] J. Cardozo, J. H. Munoz, N. Quintero, and E. Rojas, J. Phys. G: Nucl. Part. Phys. **48**, 035001 (2021) [arXiv:2006.07751 [hep-ph]] [Search inSPIRE].
[74] J. D. Gomez, N. Quintero, and E. Rojas, Phys. Rev. D **100** 093003 (2019) [arXiv:1907.08357 [hep-ph]] [Search inSPIRE].
[75] B. Y. Cui, Y. K. Huang, Y. M. Wang, and X. C. Zhao, Phys. Rev. D **108**, L071504 (2023) [arXiv:2301.12391 [hep-ph]][Search inSPIRE].
[76] K. Kojima, (Belle II Collaboration), 31st International Symposium on Lepton Photon interactions at High Energies (2023).
[77] R. Aaij et al. Phys. Rev. Lett. **131**, 111802 (2023) [arXiv:2302.02886 [hep-ph]]] [Search inSPIRE].

[78] R. Aaij et al. Phys. Rev. D **108**, 012018 (2023) [arXiv:2305.01463[hep-ph]] [Search inSPIRE].
[79] L. Zhang, X. W. Kang, X. H. Guo, L. Y. Dai, T. Luo, and C. Wang, J. High Energy Phys. **2102**, 179 (2021) [arXiv:2012.04417 [hep-ph]] [Search inSPIRE].
[80] R. N. Faustov, V. O. Galkin, and X. W. Kang, Phys. Rev. D **106**, 013004 (2022) [arXiv:2206.10277 [hep-ph]] [Search inSPIRE].
[81] R. Mandal, C. Murgui, A. Penuelas, and A. Pich, J. High Energy Phys. **2008**, 022 (2020) [arXiv:2004.06726 [hep-ph]] [Search inSPIRE].
[82] C. Murgui, A. Peñuelas, M. Jung, and A. Pich, J. High Energy Phys. **1909**, 103 (2019) [arXiv:1904.09311 [hep-ph]] [Search inSPIRE].
[83] M. Jung and D. M. Straub, J. High Energy Phys. **1901**, 009 (2019) [arXiv:1801.01112 [hep-ph]] [Search inSPIRE].
[84] M. Gonzalez-Alonso, J. Martin Camalich, and K. Mimouni, Phys. Lett. B **772**, 777 (2017) [arXiv:1706.00410 [hep-ph]] [Search inSPIRE].
[85] A. Datta, S. Kamali, S. Meinel, and A. Rashed, J. High Energy Phys. **1708**, 131 (2017) [arXiv:1702.02243 [hep-ph]] [Search inSPIRE].
[86] R. Alonso, B. Grinstein, and J. Martin Camalich, J. High Energy Phys. **1510**, 184 (2015) [arXiv:1505.05164 [hep-ph]] [Search inSPIRE].
[87] L. Calibbi, A. Crivellin, and T. Ota, Phys. Rev. Lett. **115**, 181801 (2015) [arXiv:1506.02661 [hep-ph]] [Search inSPIRE].
[88] S. Fajfer and N. Košnik, Phys. Lett. B **755**, 270 (2016) [arXiv:1511.06024 [hep-ph]] [Search inSPIRE].
[89] R. Barbieri, G. Isidori, A. Pattori, and F. Senia, Eur. Phys. J. C **76**, 67 (2016) [arXiv:1512.01560 [hep-ph]] [Search inSPIRE].
[90] R. Barbieri, C. W. Murphy, and F. Senia, Eur. Phys. J. C **77**, 8 (2017) [arXiv:1611.04930 [hep-ph]] [Search inSPIRE].
[91] G. Hiller, D. Loose, and K. Schonwald, J. High Energy Phys. **1612**, 027 (2016) [arXiv:1609.08895 [hep-ph]] [Search inSPIRE].
[92] B. Bhattacharya, A. Datta, J.-P. Guévin, D. London, and R. Watanabe, J. High Energy Phys. **1701**, 015 (2017)[arXiv:1609.09078 [hep-ph]] [Search inSPIRE].
[93] D. Buttazzo, A. Greljo, G. Isidori, and D. Marzocca, J. High Energy Phys. **1711**, 044 (2017) [arXiv:1706.07808 [hep-ph]] [Search inSPIRE].
[94] J. Kumar, D. London, and R. Watanabe, Phys. Rev. D **99**, 015007 (2019) [arXiv:1806.07403 [hep-ph]][Search inSPIRE].
[95] N. Assad, B. Fornal, and B. Grinstein, Phys. Lett. B **777**, 324 (2018) [arXiv:1708.06350 [hep-ph]] [Search inSPIRE].
[96] L. Di Luzio, A. Greljo, and M. Nardecchia, Phys. Rev. D **96**, 115011 (2017) [arXiv:1708.08450 [hep-ph]] [Search inSPIRE].
[97] L. Calibbi, A. Crivellin, and T. Li,, Phys. Rev. D **98**, 115002 (2018) [arXiv:1709.00692 [hep-ph]][Search inSPIRE].
[98] M. Bordone, C. Cornella, J. Fuentes-Martin, and G. Isidori, Phys. Lett. B **779**, 317 (2018) [arXiv:1712.01368 [hep-ph]] [Search inSPIRE].
[99] R. Barbieri and A. Tesi, Eur. Phys. J. C **78**, 193 (2018) [arXiv:1712.06844 [hep-ph]] [Search inSPIRE].
[100] M. Blanke and A. Crivellin, Phys. Rev. Lett. **121**, 011801 (2018) [arXiv:1801.07256 [hep-ph]] [Search inSPIRE].
[101] A. Greljo and B. A. Stefanek, Phys. Lett. B **782**, 131 (2018) [arXiv:1802.04274 [hep-ph]] [Search inSPIRE].
[102] M. Bordone, C. Cornella, J. Fuentes-Martín, and G. Isidori, JHEP **1810**, 148 (2018) [arXiv:1805.09328 [hep-ph]][Search inSPIRE].
[103] S. Matsuzaki, K. Nishiwaki, and K. Yamamoto, JHEP **1811**, 164 (2019) [arXiv:1806.02312 [hep-ph]][Search inSPIRE].
[104] A. Crivellin, C. Greub, F. Saturnino, and D. Muller, Phys. Rev. Lett. **122** 011805 (2019) [arXiv:1807.02068 [hep-ph]][Search inSPIRE].
[105] L. Di Luzio, F. J. Martin, A. Greljo, M. Nardecchia, and S. Renner, JHEP **11** 081 (2018)[arXiv:1808.00942 [hep-ph]][Search inSPIRE].

[106] A. Biswas, D. Kumar Ghosh, N. Ghosh, A. Shaw, and A. K. Swain, J. Phys. G: Nucl. Part. Phys. **47**, 04500 (2020) [arXiv:1808.04169 [hep-ph]][Search inSPIRE].
[107] N. G. Deshpande and A. Menon, J. High Energy Phys. **1301**, 025 (2013) [arXiv:1208.4134 [hep-ph]] [Search inSPIRE].
[108] M. Bauer and M. Neubert, Phys. Rev. Lett. **116**, 141802 (2016) [arXiv:1511.01900 [hep-ph]] [Search inSPIRE].
[109] Y. Cai, J. Gargalionis, M. A. Schmidt, and R. R. Volkas, J. High Energy Phys. **1710**, 047 (2017) [arXiv:1704.05849 [hepph]] [Search inSPIRE].
[110] A. Crivellin, D. Muller, and T. Ota, J. High Energy Phys. **1709**, 040 (2017) [arXiv:1703.09226 [hep-ph]] [Search inSPIRE].
[111] W. Altmannshofer, P. Bhupal Dev, and A. Soni, Phys. Rev. D **96**, 095010 (2017) [arXiv:1704.06659 [hep-ph]] [Search inSPIRE].
[112] D. Marzocca, J. High Energy Phys. **1807**, 121 (2018) [arXiv:1803.10972 [hep-ph]] [Search inSPIRE].
[113] X.-G. He and G. Valencia, Phys. Rev. D **87**, 014014 (2013) [arXiv:1211.0348 [hep-ph]] [Search inSPIRE].
[114] A. Greljo, G. Isidori, and D. Marzocca, J. High Energy Phys. **1507**, 142 (2015) [arXiv:1506.01705 [hep-ph]] [Search inSPIRE].
[115] S. M. Boucenna, A. Celis, J. Fuentes-Martin, A. Vicente, and J. Virto, Phys. Lett. B **760**, 214 (2016) [arXiv:1604.03088 [hep-ph]] [Search inSPIRE].
[116] X.-G. He and G. Valencia, Phys. Lett. B **779**, 52 (2018) [arXiv:1711.09525 [hep-ph]] [Search inSPIRE].
[117] J. Kalinowski, Phys. Lett. B **245**, 201 (1990).
[118] W.-S. Hou, Phys. Rev. D **48**, 2342 (1993).
[119] N. Kosnik, Phys. Rev. D **86**, 055004 (2012) [arXiv:1206.2970 [hep-ph]] [Search inSPIRE].
[120] A. Biswas, A. Shaw, and A. K. Swain, Lett. High Energy Phys., **2**, 126 (2019) [arXiv:1811.08887 [hep-ph]][Search inSPIRE].
[121] A. Crivellin, C. Greub, and A. Kokulu, Phys. Rev. D **86**, 054014 (2012) [arXiv:1206.2634 [hep-ph]] [Search inSPIRE].
[122] A. Crivellin, A. Kokulu, and C. Greub, Phys. Rev. D **87**, 094031 (2013) [arXiv:1303.5877 [hep-ph]] [Search inSPIRE].
[123] A. Celis, M. Jung, X.-Q. Li, and A. Pich, J. High Energy Phys. **1301**, 054 (2013) [arXiv:1210.8443 [hep-ph]] [Search inSPIRE].
[124] P. Ko, Y. Omura, and C. Yu, J. High Energy Phys. **1303**, 151 (2013) [arXiv:1212.4607 [hep-ph]] [Search inSPIRE].
[125] A. Crivellin, J. Heeck, and P. Stoffer, Phys. Rev. Lett. **116**, 081801 (2016) [arXiv:1507.07567 [hep-ph]] [Search inSPIRE].
[126] L. Dhargyal, Phys. Rev. D **93**, 115009 (2016) [arXiv:1605.02794 [hep-ph]] [Search inSPIRE].
[127] C.-H. Chen and T. Nomura, Eur. Phys. J. C **77**, 631 (2017) [arXiv:1703.03646 [hep-ph]] [Search inSPIRE].
[128] S. Iguro and K. Tobe, Nucl. Phys. B **925**, 560 (2017) [arXiv:1708.06176 [hep-ph]] [Search inSPIRE].
[129] R. Martinez, C. F. Sierra, and G. Valencia, Phys. Rev. D, **98**, 115012 (2018) [arXiv:1805.04098 [hep-ph]] [Search inSPIRE].
[130] A. Biswas, D. K. Ghosh, A. Shaw, and S. K. Patra, Int. J. Mod. Phys. A **34**, 1950112 (2019) [arXiv:1801.03375 [hep-ph][Search inSPIRE].
[131] A. Greljo, J. Martin Camalich, and J. D. Ruiz-Alvarez, Phys. Rev. Lett. **122**, 131803 (2019) [arXiv:1811.07920 [hep-ph]] [Search inSPIRE].
[132] M. Endo, S. Iguro, T. Kitahara, M. Takeuchi, and R. Watanabe, J. High Energy Phys. **2202**, 106 (2022) [arXiv:2111.04748 [hep-ph]] [Search inSPIRE].